The influence of heat transfer and friction on the impulse of a detonation tube

著者	Kawane Ko, Shimada Satoshi, Kasahara Jiro, Matsuo Akiko
journal or publication title	Combustion and flame
volume	158
number	10
page range	2023-2036
year	2011-10
権利	(C) 2011 The Combustion Institute. Published by Elsevier Inc. NOTICE: this is the author's version of a work that was accepted for publication in Combustion and flame. Changes resulting from the publishing process, such as peer review, editing, corrections, structural formatting, and other quality control mechanisms may not be reflected in this document. Changes may have been made to this work since it was submitted for publication. A definitive version was subsequently published in PUBLICATION, Volume 158, Issue 10, October 2011, Pages 2023-2036 DOI:10.1016/j.combustflame.2011.02.017
URL	http://hdl.handle.net/2241/114064

doi: 10.1016/j.combustflame.2011.02.017

1. Title:

The influence of heat transfer and friction on the impulse of a detonation tube

2. Authors and affiliations:

Ko Kawane[1], Satoshi Shimada[1], Jiro Kasahara[1], and Akiko Matsuo[2]

[1]Department of Engineering Mechanics and Energy
University of Tsukuba
1-1-1 Tennodai, Tsukuba, 305-8573, Japan
[2]Department of Mechanical Engineering
Keio University
3-14-1 Hiyoshi, Kohoku-ku, Yokohama, 223-8522, Japan

3. Corresponding author's complete contact information:

Mailing address:
Jiro KASAHARA, Department of Engineering Mechanics and Energy
University of Tsukuba, 3D bldg. room 116, 1-1-1 Tennodai, Tsukuba, 305-8573, Japan
Phone, Fax: +82-029-853-5267
Email: kasahara@kz.tsukuba.ac.jp

Abstract

In the present study, we experimentally and numerically investigated the influence of heat transfer and friction on the performance of a single-shot detonation tube open at one end. Two kinds of specific impulse measurement were carried out with various tube lengths and levels of surface roughness, one by using a ballistic pendulum arrangement and the other by integrating the pressure history measured at the thrust wall. These measurements revealed the degree to which potential impulse can be exploited by the detonation tube after the impulse losses due to various wall loss mechanisms such as heat transfer and friction. The detonation tube obtained 89%, 70%, and 64% of the theoretical ideal impulse for electropolished tubes at a ratio of tube length to diameter (*L/D*) of 49, 103, and 151, respectively. The impulse losses due to shear stress on the side wall of the detonation tube were found to have a dominant influence on the performance of the detonation tubes of *L/D*=103 and 151, but the loss was remarkably small for *L/D*=49 relative to that of the longer tubes. In addition to the experiments, a simplified one-dimensional gas-dynamic model was developed by considering heat transfer and friction as wall loss mechanisms and validated by the experimental results. This simplified model was found to predict the experimental results very well, especially in the range of *L/D* 103 to 151.

Keywords

Detonation, Pulse Detonation Engine, Detonation Tube, Heat Transfer, Friction

Nomenclature

A	=	a/a_{CJ}, nondimensional sound velocity
a	=	sound velocity
c_p	=	specific heat at constant pressure
C_f	=	friction coefficient
C_h	=	heat transfer coefficient
D	=	tube diameter
D_{CJ}	=	detonation velocity
f	=	shear stress per unit mass
g	=	gravitational acceleration
I	=	impulse
$I_{end\text{-}wall}$	=	impulse obtained as the integral of the pressure history at the thrust wall
$I_{pressure\text{-}deficit}$	=	impulse loss emerging as the pressure deficit due to heat transfer and friction
I_{isen}	=	ideal impulse obtained using isentropic flow assumption
$I_{net\text{-}thrust}$	=	impulse obtained in the method of a ballistic pendulum
$I_{shear\text{-}stress}$	=	impulse loss due to shear stress
I_{sp}	=	specific impulse
L	=	tube length
l_w	=	effective wire length
M	=	number of discrete segments for the initial Taylor expansion wave
m_{prop}	=	propellant mass
m_t	=	tube mass
m_w	=	wire mass
N	=	number of discrete segments on the C_+ characteristic corresponding to the detonation wave
Pr	=	Prandtl number
p	=	pressure
p_{pl}	=	plateau pressure
q	=	heat loss per unit mass

R	=	ideal-gas constant
R_a	=	arithmetical mean roughness
r	=	distance from the supporting point of the wire
S	=	$s/\Gamma R$, nondimensional entropy
s	=	entropy
T	=	temperature
T^0	=	stagnation temperature
T_w	=	wall temperature
t	=	time from detonation initiation at the closed end of the tube
t_{cyc}	=	time when the pressure at the closed end of the tube decays to the ambient level
t_t	=	time when the rear boundary of the Taylor wave arrives at the open end of the tube
t^*	=	time when the exhausting rarefaction wave arrives at the closed end of the tube
t_{ws}	=	time when the pressure at the open end of the tube decays to the ambient level
U	=	u/a_{CJ}, nondimensional particle velocity
u	=	particle velocity
v_0	=	initial velocity of the detonation tube
x	=	distance from the closed end of the tube
x_{imp}	=	initial displacement of the impactor
x_m	=	horizontal maximum displacement of the ballistic pendulum
Γ	=	isentropic index
γ	=	specific heat ratio
$\eta_{end\text{-}wall}$	=	$I_{sp,end\text{-}wall}/I_{sp,isen}$, specific impulse efficiency
$\eta_{net\text{-}thrust}$	=	$I_{sp,net\ thrust}/I_{sp,isen}$, specific impulse efficiency
ρ	=	gas density
ρ_w	=	linear density of wires
τ	=	ta_{CJ}/L, nondimensional time
τ_w	=	shear stress per unit surface
ξ	=	x/L, nondimensional distance

Ψ = nondimensional shear stress per unit mass

I. Introduction

A pulse detonation engine (PDE) obtains thrust by generating detonation waves intermittently [1, 2]. PDEs have recently been recognized as a potential aerospace propulsion system [3, 4] and were demonstrated as a rocket system by Kasahara et al. [5]. The basic structure of a PDE is a straight circular tube with one end closed and the other end open. Figure 1 shows a schematic diagram of the general PDE cycle. The tube is initially filled with a combustible mixture of reactants [Fig. 1(a)] and ignited at the closed end [Fig. 1(b)]. A detonation wave is initiated there and propagates through the reactants, leaving a mixture of high-pressure combustion products behind the wave [Fig. 1(c)]. The detonation wave exits as a strong blast wave into the surrounding air, and then the high-pressure products in the tube expand and are exhausted from the tube, allowing the pressure in the tube to decay to the ambient level [Fig. 1(d)]. A PDE obtains thrust in the opposite direction from that of the blowdown of the exhaust gas at this stage. Finally, to return to the initial condition of the cycle, the combustion products are purged from the tube by replacing them with inert gases [Fig. 1(e)].

The PDE system has potential advantages compared to conventional aero-propulsion systems in reduced mechanical complexity, high thermodynamic efficiency, and high specific impulse (I_{sp}). Since unburned gas is compressed by a shock wave before combustion, the PDE is able to produce high-enthalpy gas without a complex compression mechanism, which is necessary for conventional propulsion systems. In addition, since the isovolumetric combustion takes place due to the detonation wave propagating at hypersonic speed, the performance of the PDE should be higher than that of systems using the Humphrey cycle (isovolumetric combustion cycle) and Brayton cycle (isobaric combustion cycle) in the case of an airbreathing PDE [6] and pulse detonation turbine engine. Moreover, it is easy to increase the performance by using simple mechanisms, such as an extension tube for partial filling (Sato et al. [7], Endo et al. [8], Kasahara et al. [9, 10]) and a nozzle (Morris [11]).

For simplicity, in the primary stage of studies on PDEs, a detonation tube (DT) that produces a single detonation wave is typically used to estimate the performance of PDEs, and its single-shot specific impulse, I_{sp}, is often used as a performance metric. Endo et al. [12, 13] analytically and Wentenberger et al. [14] quasi-analytically/quasi-empirically predicted the flow field inside the tube and calculated the performance of the DT under the assumption that the flow inside the tube is isentropic. However, a number of different experiments have shown that the measurement values of I_{sp} of the DT are lower than the analytical values (Takeuchi et al. [15], Laviolette et al. [16], Kasahara et al. [17]). We believe there are two reasons for this. The first reason is the influence of the initiation

process of the detonation wave. In the analytical models proposed by Endo et al. and Wintenberger et al., the detonation wave is assumed to be directly initiated at the closed end of the tube, which is different from the actual flow in which the detonation wave is initiated through a so-called deflagration-to-detonation transition (DDT). In the case when the detonation wave occurs just inside the exit of the tube through the DDT, acoustic waves caused by the expansion of the detonation products reach the exit of the DT prior to the detonation wave, resulting in spillage of the propellant and hence an impulse deficit (Takeuchi et al. [15], Harris et al. [18], Kiyanda et al. [19]). The second reason is the influence of wall loss mechanisms such as heat transfer and friction, and this influence is the primary theme of the present study and has been the theme of several previous studies. Sichel and David [20] applied the analysis of the shock tube boundary layer proposed by Mirels [21] and Hartunian et al. [22] to the boundary layer behind a detonation wave moving past a flat plate and predicted the heat flux there with the assumption that the flow field behind the detonation wave is steady and constant. Using a modified Reynolds analogy in their model, Sichel and David related the heat flux to the shear stress. Skinner [23] analyzed the flow field in the tube one-dimensionally by the method of characteristics and by applying a Reynolds analogy to the non-steady Taylor expansion to investigate the influence of the heat flux and shear stress. Edwards et al. [24] experimentally observed the pressure and velocity deficits behind the detonation wave caused by the effect of heat losses. Edwards' pressure, velocity, and heat flux measurements confirmed the analysis models of Sichel and David [20] and Skinner [23].

In recent years, in response to the expectations regarding the practical application of PDEs, many experimental and numerical studies evaluating the thrust of PDEs have been performed. Laviolette et al. [16] experimentally found that the specific impulse generated in the DT remarkably decreases as the tube aspect ratio of length to diameter, L/D, increases. They explained these results with the simple analytical model of a flow field and showed that the heat losses and frictional losses have a dominant influence on the performance of the DT. Kasahara et al. [17] and Kojima [25] confirmed that the specific losses due to heat transfer increase exponentially with increasing L/D by conducting experiments in very long tubes. Radulescu and Hanson [26] calculated the flow field of the DT with the non-steady physical model proposed by Skinner [23] and predicted how the specific impulse changes with increasing L/D. In their study, they considered only heat transfer as wall losses. Their model is in good agreement with the pressure and specific impulse measurements conducted in a number of different experiments. Owens and Hanson [27] developed the one-dimensional model initially proposed by Owens et al. [28] and Mattison et al. [29] by considering heat conduction in addition to heat convection and friction. They confirmed the validity of their

model by comparing the heat flux and shear stress predicted by their model with those predicted by the Navier-Stokes model. Moreover, they showed with experiments and a one-dimensional model that in addition to heat transfer and friction, water condensation at the cold wall whose surface temperature is below the saturation temperature significantly attenuates the pressure in the tube and, as a result, the specific impulse. Barbour and Hanson [30] predicted that losses due to chemical non-equilibrium caused at the nozzle attached to the straight tube decrease the performance of the DT, because when the combustion product expands strongly there, the combustion products are not allowed to reach chemical equilibrium, thereby inhibiting chemical recombination and its associated heat release. In the straight tube without a nozzle, on the other hand, the influence of chemical non-equilibrium is within the error of measurement and can be neglected.

Many experimental and numerical studies of the impulse losses emerging as the pressure declines have been performed by evaluating the pressure profile at the thrust wall. However, there is no experimental data that indicates how much impulse is lost due to shear stress on the side wall in the direction opposite from that of the thrust at the end wall and hence how much force remains after that. Figure 2 is a schematic diagram of these forces. Previous experimental measurements of specific impulse conducted by Harris et al. [18] with a DT of L/D=49.5 showed that the pressure integral on the thrust wall agrees, within experimental accuracy limits, with measurements utilizing a ballistic pendulum, which integrates all of the forces acting on the side and end walls, and this result indicated that skin friction on the side walls of the tube might have only a negligible influence on impulse. On the other hand, a recent numerical study by Owens and Hanson [27] revealed that shear stress has a dominant influence on the performance of a DT. In the present study, we conducted single-shot experiments similar to those of Harris et al. [18] with a wide range of L/D (50-250) to evaluate the momentum losses due to the shear stress as the difference between the pressure-based specific impulse and the net specific impulse obtained with the ballistic pendulum arrangement. Furthermore, with the simplified physical model considering only heat transfer and friction, we calculated the flow field inside the DT using methods similar to those of Skinner [23] and Radulescu and Hanson [26] and compared the simulation results with the experimental measurements in the wide range of L/D. Although heat transfer and friction are essential wall loss mechanisms, the model considering them alone has never been validated by measured experimental data. We validated the model by experimental results for the first time.

II. Outline of Experimental Approach and Equipment

A. Experimental Approach

To evaluate the specific impulse losses, we performed single-shot experiments and measured impulse obtained by the DT in the following two ways.

First, since the DT obtains thrust by the high-pressure detonation product pushing against the end wall, the impulse can be calculated by integrating the pressure history at the end wall, as follows:

$$I_{\text{end wall}} = \pi\left(\frac{D}{2}\right)^2 \int_0^{t_{\text{cyc}}} (p_{\text{w}} - p_0)\,\mathrm{d}t \tag{1}$$

For the end time of the integral, we use t_{cyc}, that is, the time after ignition when the pressure at the closed end of the tube first decays to the ambient level.

The second way of measuring the momentum is to use the ballistic pendulum arrangement, which was first proposed by the Nicholls et al [1]. In this method, the DT is hung from the ceiling with wires, and the horizontal maximum displacement, x_{m}, of the DT is measured to calculate the initial velocity, v_0, of the DT at the lowest point of the pendulum movement. From elementary mechanics, the initial velocity of the DT is determined as follows [18, 19]:

$$v_0 = \sqrt{2gl_w\left(1 - \sqrt{1 - \left(\frac{x_{\text{m}}}{l_w}\right)^2}\right)} \tag{2}$$

This formula is based on the assumptions that the DT gets the impulsive force and starts the pendulum movement at the lowest point, since the impulsive force duration is much shorter than the pendulum cycle, and that the kinetic energy of the DT converts to the potential energy as the pendulum moves up, under the law of conservation of mechanical energy. The momentum of the DT, $I_{\text{net-thrust}}$, can be obtained as the product of the velocity, v_0, and the mass of the pendulum and wires, m_{t} and m_{w}, respectively, as follows:

$$I_{\text{net thrusst}} = \int_0^{l_w} \frac{r}{l_w} v_0 \rho\,\mathrm{d}r + m_{\text{t}} v_0 = \left(\frac{1}{2}m_{\text{w}} + m_{\text{t}}\right)v_0 \tag{3}$$

To evaluate the losses in performance of the DT in addition to these two kinds of momentum, we use the impulse, I_{isen}, from the ideal theory that the flow field is assumed to be isentropic. In the actual flow field measured in the

experiments, the pressure-based impulse, $I_{\text{end-wall}}$, is less than the ideal impulse, I_{isen}. This is because of the influence of heat transfer and friction, which emerges as the pressure deficit at the thrust wall. We relate these impulses with the following equations:

$$I_{\text{end-wall}} = I_{\text{isen}} + I_{\text{pressure-deficit}}$$

$$I_{\text{pressure-deficit}} = I_{\text{end-wall}} - I_{\text{isen}} \tag{4}$$

where the impulse in the thrust direction is a positive quantity and the corresponding impulse related to reduce the thrust, such as $I_{\text{pressure-deficit}}$, is a negative value.

Comparing $I_{\text{end-wall}}$ with $I_{\text{net-thrust}}$, we expect the latter to be less, because the impulses acting on the DT are not only $I_{\text{end-wall}}$ but also the negative impulse on the side wall, $I_{\text{side-wall}}$, which is caused by the shear stress generated by the fast-exhausting detonation product. This relationship is expressed as follows:

$$I_{\text{net-thrust}} = I_{\text{end-wall}} + I_{\text{side-wall}}$$

$$I_{\text{side-wall}} = I_{\text{net-thrust}} - I_{\text{end-wall}} \tag{5}$$

Since in the present study we conducted experiments with various tube lengths as a parameter, it is appropriate to evaluate the impulse losses per unit of propellant weight. Consequently, we converted the previous impulses to the specific impulse, as follows.

$$I_{\text{sp}} = \frac{I}{m_{\text{prop}} g} \tag{6}$$

B. Experimental Equipment

A schematic of the experimental apparatus is shown in Fig. 3, and a photograph of the experimental devices is presented in Fig. 4. We used the same experimental equipment as was described in our previous study [31]. The diameter, D, of the DT is fixed at 25.5 mm, and the tube length, L, and the surface roughness. R_{a}. of the tube wall were used as the experimental variables. Dividing by the diameter, D, these parameters are evaluated as the ratios L/D and R_{a}/D. Table 1 shows the details of the seven experimental conditions used in the present study. At the shot conditions from P1 to P3, we used tubes whose internal surface was electropolished (polished tubes, R_{a}/D = 5.00×10^{-5}) with tube lengths of 1237, 2635, and 3841 mm (L/D = 49, 103, and 151, respectively). Note that the tube used at P3 is composed of the coupled tubes used at P1 and P2. For the shot conditions from N1 to N3, we used

tubes whose internal surface was not polished (normal tubes, $R_a/D = 1.96\times10^{-4}$) with the same tube lengths as the polished tubes.

To conduct experiments with an extremely long tube, we arrange shot condition LT (long tube) with the coupled tubes used at P1, P2, and N2. To configure the ballistic pendulum arrangement, the DT is hung from the ceiling with stainless wires whose length, l_w, is 2704.8±2.6 mm. The wires are put in a V-formation, as shown on the left side of Fig. 3, to make the tube move in the axial direction. The location and position of the tube is fine-adjusted by changing the wire length with the turnbuckles attached to all wires. The tubes with an L/D of 49 and 103 are hung at two points, and that with an L/D of 151 is hung at three points. For shot condition LT, we do not use the ballistic pendulum method. That is, the DT is not hung from the ceiling but rather is fixed on the ground.

In this experiment, the stoichiometric C_2H_4-O_2 mixture in the standard condition is used as the propellant. This mixture was allowed to diffusively mix for at least 24 hours in a high-vacuum pre-mixing tank. The stoichiometry of the mixture was determined by the method of partial pressures. The open end of the tube is sealed with a 1.5-μm-thick polyethylene terephthalate diaphragm, which prevents inflow of the ambient gas when the DT is evacuated to high vacuum as well as diffusion of the propellant after the filling. This diaphragm is ruptured by the arrival of the detonation wave and has momentum in the axial direction following gas exhaustion. The DT gets additional momentum as a result of this reaction. In this experiment [31], to reduce the contribution of the diaphragm to the momentum of the tube, we made a device to enable us to use a diaphragm that is one-tenth the thickness of previously used diaphragms. A port for inlet and outlet is installed at the side wall near the tube end to evacuate the DT and supply the propellant. This port is connected to the pre-mixing tank through a valve and quick release joint, as shown in Fig. 4, which enables the gas supply pipe to be separated from the tube during the ballistic pendulum experiments. The propellant mixture is ignited with a spark plug at the end wall of the tube. The high voltage necessary for the electric spark is obtained by raising the 12-V DC power with an ignition coil. First, the deflagration is generated by an electric spark, producing a detonation wave. To accelerate this transition, we installed a Shchelkin spiral (50 mm long with a blockage ratio of 0.42) at the closed end of the tube. We installed three piezoelectric pressure transducers at the right, bottom, and left side surfaces 5 mm from the thrust wall, as shown in Fig. 3. Since 5 mm is much less than the tube length, we considered the measured profile to be the pressure history at the thrust wall. These transducers are isolated from the hot detonation products with a thin layer of high-temperature silicon grease. Taking measurements at three points plays an important role in improving the reliability

of measurements. In addition to the end wall, the DT of shot condition N3 is fitted with three pressure transducers at the side wall of x/L = 0.374, 0.661, and 0.948 from the end wall. These transducers are also isolated with silicon grease. The maximum horizontal displacement, x_m, of the ballistic pendulum is measured by a laser displacement sensor and a video camera, with which a ruler attached to the DT is captured. The shooting frequency of the video camera was 300 Hz.

Accurate calculation of the momentum of the tube by the ballistic pendulum method depends on the accurate measurement of the tube mass, m_t, of the DT and the initial velocity, v_0. However, it is difficult to eliminate the influence of conductor wires for the measurement apparatuses and ignition system. We conducted preliminary experiments with an impactor to calibrate the impulse acting on the DT. This calibration method with an impactor is new and has only been used by the authors' group [15]. The goal of this preliminary experiment was to relate the maximum horizontal displacement of the DT to the known I_{sp}. Figure 5 shows the schematic of this experiment. Since the impactor is a pendulum without any resistance such as that caused by conducting wires, it has a known momentum right before the collision, calculated as follows:

$$I_{imp} = \left(\frac{1}{2}m_w + m_{imp}\right)\sqrt{2gl\left(1-\sqrt{1-\left(\frac{x_{imp}}{l}\right)^2}\right)} \tag{7}$$

where x_{imp} is the displacement from the initial rest point to the collision point.

After the collision, the impactor and the DT couple and continue oscillating, as shown in the lower part of Fig. 5. The coupled pendulum obtains momentum equal to I_{imp} under the law of conservation of momentum and comes to rest at the highest point after a certain horizontal displacement, x_m. In this experiment, x_{imp} and x_m are measured with the laser displacement sensor. We conducted the same experiments repeatedly with various momenta and plotted the results on the $I_{sp,imp}$ versus x_m graph to relate the maximum horizontal displacement to the known specific impulse with the linear relationship, where $I_{sp,imp}$ is obtained by dividing Eq. (7) by the propellant weight used in the corresponding DT experiments. As an example, Fig. 6 shows the graph in the case of the P3 condition. In the single-shot experiments, the DT starts to oscillate due to the specific impulse, $I_{sp,net\text{-}thrust}$, and moves distance x_m. Calculating the corresponding value of I_{sp} from the linear relationship with x_m,, we can easily determine $I_{sp,net\text{-}thrust}$ without considering the tube mass, m_t, or the initial velocity, v_0.

The impactor is hung with wires put in a V-formation. We used wires of the same length as those for the DT, because the period of vibration should be equal. For the joint of the DT and the impactor, we used a magnet. Even though both the DT and the impactor accelerate before collision due to magnetic attraction, Eq. (7) is valid, since the internal force does not affect the law of conservation of momentum.

Figure 7 shows the difference in $I_{sp,net\text{-}thrust}$ before and after the calibration. The solid line shows $I_{sp,net\text{-}thrust}$ without calibration. In the case with long tubes such as P2, N2, P3, and N3, the plots agree well with the solid line. On the other hand, in the case with short tubes such as P1 and N1, the plots deviate from the solid line. This suggests the possibility that tubes with small mass are subject to the resistance of conducting wires, and the traditional ballistic pendulum approach cannot predict I_{sp} successfully in such a situation.

III. Model Description

To interpret the experimental data and obtain additional insight into the flow field of the DT, we developed a simplified computational model. Numerous researchers have developed both simple and complex simulations designed to predict and evaluate PDE performance, in which many wall loss mechanisms were found to affect the flow field of the DT, for example, convective heat transfer (Skinner [23], Radulescu and Hanson [26], Owens and Hanson [27], Barbour and Hanson [30]), conductive heat transfer [27 ,30], wall shear stress [23, 27, 30], water condensation [27], and chemical recombination [27, 30]. In the present study, similar to the study by Skinner [23], we adopted convective heat transfer and wall shear stress as wall loss mechanisms. Although these two mechanisms are essential dominant factors, the model considering them alone has never been validated by measured experimental data. In the following section we describe the details of this simplified model and evaluate its validity for the first time.

In this model, the burned gas is assumed to be the thermally perfect polytropic gas. Although in the actual flow the polytropic exponent is variable, depending on the chemical equilibrium, the variation width is known to be less than 1% through the strong expansion behind the detonation wave in ethylene-oxygen products [32, 33], and consequently in this model it is assumed to be fixed to the value for the Chapman-Jouguet (CJ) state. Instead of the specific ratio γ, we use the isentropic exponent Γ, which is the polytropic exponent when the flow is changed along the chemical equilibrium isentrope. Γ is determined as follows:

$$\Gamma = \left(\frac{\partial \ln p}{\partial \ln \rho} \right)_s \tag{8}$$

Under the approximation that the transport of energy and momentum due to heat conduction and viscosity between flow particles is neglected, the flow field is described with a one-dimensional Euler's equation. The transport of momentum and energy due to wall losses is treated as a set of volumetric source terms without taking into account the gradients of momentum and temperature.

The wall shear stress per unit mass, f, is given as follows with the frictional coefficient C_f:

$$f = \frac{2C_f u|u|}{D} \tag{9}$$

Similar to several previous studies (Radulescu and Hanson [26], Owens and Hanson [27], Barbour and Hanson [30]), we used C_f as a constant, 0.0062, behind the detonation wave. This approximation is widely recognized as being not entirely arbitrary, since in turbulent flows C_f approaches a constant value at high Reynolds numbers. The convective heat transfer, q, per unit mass is given as follows with the heat transfer coefficient C_h:

$$q = -\frac{4C_h}{\rho D}\left(T^0 - T_w\right) \tag{10}$$

where T^0 is given as follows:

$$T^0 = \left(1 + \frac{\Gamma - 1}{2}\frac{u^2}{a^2}\right)T \tag{11}$$

T_w is assumed to be constant and equal to the ambient temperature for the entire process. Similar to several previous studies, we assume the Reynolds analogy [34] between heat transfer and friction, and relate the heat transfer coefficient, C_h, and the frictional coefficient, C_f, as follows:

$$\frac{C_h}{\rho c_p u} Pr^{2/3} = \frac{C_f}{2} \tag{12}$$

The Prandtl number, Pr, is assumed to be constant and is computed using Eucken's formula [35], as follows:

$$Pr = \frac{4\Gamma}{9\Gamma - 5} \tag{13}$$

Since the isentropic exponent, Γ, is 1.14 for the ethylene-oxygen detonation product, the Prandtl number, *Pr*, is equal to 0.87.

Incorporating the continuity equation and the energy equation into the one-dimensional Euler's equation and writing it in non-dimensional form, we obtain the characteristic equation in which we choose the particle velocity, sound velocity, and entropy as dependent variables, as follows:

$$\frac{\mathrm{D}_{\pm}}{\mathrm{D}\tau}\left(\frac{2}{\Gamma-1}A\pm U\right)=A\frac{\mathrm{D}_{\pm}S}{\mathrm{D}\tau}+(\Gamma-1)A\frac{\mathrm{D}S}{\mathrm{D}\tau}\pm\Psi \tag{14}$$

where

$$\frac{\mathrm{D}_{\pm}}{\mathrm{D}\tau}\equiv\frac{\partial}{\partial\tau}+(U\pm A)\frac{\partial}{\partial\xi} \tag{15}$$

$$\frac{\mathrm{D}}{\mathrm{D}\tau}\equiv\frac{\partial}{\partial\tau}+U\frac{\partial}{\partial\xi} \tag{16}$$

The capitalized variables represent the non-dimensional quantities, taking the CJ state as a reference.

Equation (15) contains differential operators for calculating the time variation of parameters in the coordinate system, which moves along with fluid particles at speeds $U\pm A$ and U, respectively, where $U\pm A$ is the velocity of small perturbations generated as the flow particles move at speed U and propagate forward and backward. Here, Ψ is the non-dimensional form of the wall shear stress, f. A detailed description of the characteristic equation is found in Ref. 36.

To integrate Eq. (14), it is necessary to examine the details of Ds/Dτ, that is, the entropy variation in the coordinate system, which moves along with fluid particles and stems from the two kinds of energy loss described previously. One is the dissipation of kinetic energy due to friction, and the other is the heat transfer, q, to the side wall of the DT. Ds/Dτ is calculated as follows:

$$\frac{\mathrm{D}S}{\mathrm{D}\tau}=\left(\frac{\mathrm{D}S}{\mathrm{D}\tau}\right)_{\text{Friction}}+\left(\frac{\mathrm{D}S}{\mathrm{D}\tau}\right)_{\text{Heat Transfer}}$$

$$\frac{\mathrm{D}S}{\mathrm{D}\tau}=-\frac{C_{\mathrm{f}}|U|}{(\Gamma-1)A^2}\frac{L}{D}\left[\frac{1}{Pr^{2/3}}\left(A^2+\frac{\Gamma-1}{2}U^2-1\right)-(\Gamma-1)U^2\right] \tag{17}$$

These three characteristic equations given by Eq. (14) and Eq. (17) become ordinary differential equations along the three families of characteristics C_+, C_- and C_0 given by

$$C_\pm : \frac{\mathrm{d}\xi}{\mathrm{d}\tau} = U \pm A \tag{18}$$

$$C_0 : \frac{\mathrm{d}\xi}{\mathrm{d}\tau} = U \tag{19}$$

We use the intersections of these characteristics to configure grid points, and equations (14) and (17) can be integrated numerically using a finite difference scheme in the domain covered by the net of characteristics $C_\pm$. This numerical scheme is called the method of characteristics, and one of its advantages is that there is no need for a predefined grid. Figure 8 illustrates the resultant net of characteristics on the ξ-τ plane within the inside tube ($0 \le \xi \le 1$). Eqs. (14), (17), (18), and (19) can be written in discretized form in the interior domain, free from detonation wave and boundary interactions. A sketch of an example of the grid construction in the interior domain on the ξ-τ plane is shown in Fig. 9a. Points 1 and 2 are two points at which all flow conditions are known. Point 3 lies at the intersection of the C_+ characteristic through point 1 and the C_- characteristic through point 2. The characteristic lines are assumed to be straight-line segments linking two successive grid points. The particle pathline C_0 through point 3 intersects line 1-2 at point 4. Knowing the solution at points 1 and 2, that is, (ξ_1, τ_1, S_1, U_1, A_1, ξ_2, τ_2, S_2, U_2, A_2), the solution at points 3 and 4, that is, (ξ_3, τ_3, S_3, U_3, A_3, ξ_4, τ_4, S_4, U_4, A_4), satisfies the discretized version of the $C_\pm$ characteristic equations (14),

$$\begin{aligned} &\frac{2}{\Gamma-1}\left(A_3 - A_1\right) + \left(U_3 - U_1\right) = \\ &A_{13}\left(S_3 - S_1\right) - \frac{C_\mathrm{f}\left|U_{13}\right|}{A_{13}}\frac{L}{D}\left[\frac{1}{\mathrm{Pr}^{2/3}}\left(A_{13}{}^2 + \frac{\Gamma-1}{2}U_{13}{}^2 - 1\right) - (\Gamma-1)U_{13}{}^2 + U_{13}A_{13}\right]\left(\tau_3 - \tau_1\right) \end{aligned} \tag{20}$$

$$\begin{aligned} &\frac{2}{\Gamma-1}\left(A_3 - A_2\right) - \left(U_3 - U_2\right) = \\ &A_{23}\left(S_3 - S_2\right) - \frac{C_\mathrm{f}\left|U_{23}\right|}{A_{23}}\frac{L}{D}\left[\frac{1}{\mathrm{Pr}^{2/3}}\left(A_{23}{}^2 + \frac{\Gamma-1}{2}U_{23}{}^2 - 1\right) - (\Gamma-1)U_{23}{}^2 - U_{23}A_{23}\right]\left(\tau_3 - \tau_2\right) \end{aligned} \tag{21}$$

the entropy equation (17),

$$S_3 - S_4 = -\frac{C_\mathrm{f}\left|U_{34}\right|}{(\Gamma-1)A_{34}{}^2}\frac{L}{D}\left[\frac{1}{\mathrm{Pr}^{2/3}}\left(A_{34}{}^2 + \frac{\Gamma-1}{2}U_{34}{}^2 - 1\right) - (\Gamma-1)U_{34}{}^2\right]\left(\tau_3 - \tau_4\right) \tag{22}$$

and the C_+, C_- [Eq. (18)] and C_0 [Eq. (19)] characteristics

$$\frac{\xi_3-\xi_1}{\tau_3-\tau_1}=U_{13}+A_{13} \tag{23}$$

$$\frac{\xi_3-\xi_2}{\tau_3-\tau_2}=U_{23}-A_{23} \tag{24}$$

$$\frac{\xi_3-\xi_4}{\tau_3-\tau_4}=U_{34} \tag{25}$$

where a double subscript, such as A_{13}, means that the flow parameters are averaged between respective points. More detailed descriptions of the calculation can be found in Ref. 23.

The initial and boundary conditions we used are similar to those presented by Radulascu and Hanson [26]. The flow field on the first C_- characteristics for the Taylor expansion is given in the analytical solution for isentropic flows by Endo et al. [12]. We assume the detonation wave propagates at a constant velocity in the CJ condition. Since the CJ detonation wave velocity in the rest coordinate system is the sum of the flow velocity and the sonic velocity of the CJ state, i.e., $D_{CJ}=u_{CJ}+a_{CJ}$, the detonation wave becomes the first C_+ characteristic, as shown in Fig. 8 with the thick solid line. The quantities of the CJ condition are obtained by AISTJAN [37], which is used for chemical equilibrium calculations.

At the closed-end wall, we assume the gas is at rest, with the following conditions:

$$\xi=0 : U=0,\ S=S_{CJ} \tag{26}$$

At the open end of the DT, the flow velocity is assumed to be always at sonic velocity, with the following conditions:

$$\xi=1 : U=A \tag{27}$$

With these initial and boundary conditions, the flow solutions for the detonation wave and boundary lines are also written in the discretized form. In Fig. 8, the path of the detonation wave is shown with a thick line, and it is represented by 11 discrete points for clarity. Assuming the number of discrete points on the detonation wave to be N+1, we can write the flow conditions of the n-th point from the end wall as follows:

$$A_n=1,\ U_n=U_{CJ},\ S_n=S_{CJ},\ \xi_n=n/N,\ \tau_n=a_{CJ}/D_{CJ}*n/N \tag{28}$$

In addition to the number of discrete points, N, on the detonation wave, we need another index to determine the degree of spatial and temporal resolution of the calculation domain. We divide the initial Taylor expansion fan equiangularly into M segments. In Fig. 8, M=10 for clarity.

Figs. 9(b) and (c) are sketched examples of the grid construction at the closed-end wall and the open end of the DT. At the closed-end wall shown in Fig. 9(b), particle pathline C_0 overlaps with the ξ=0 line, and the flow solution at point 3 is written only with the solution at point 2, as follows:

$$A_3 = A_2 - \frac{\Gamma - 1}{2}\left[U_2 - A_{23}\left(S_3 - S_2\right)\right] \tag{29-1}$$

$$U_3 = 0 \tag{29-2}$$

$$S_3 = S_{\mathrm{CJ}} \tag{29-3}$$

$$\xi_3 = 0 \tag{29-4}$$

$$\tau_3 = \tau_2 - \frac{\xi_2}{U_2 - A_{23}} \tag{29-5}$$

At the open end shown in Fig. 9(c), the C_- characteristic overlaps with the ξ=1 line, and the flow solution at point 3 can be derived from Eqs. (20)-(25) by substituting U_2=A_2 and ξ_3=1.

In Fig. 8, the interval between the lines of the detonation wave and the next C_+ characteristic expands more remarkably than other intervals in Taylor expansion. This is because strong expansion occurs immediately behind the detonation wave. Similar to Skinner [23] and Radulascu and Hanson [26], we introduce new C_+ characteristics (not shown in Fig. 8) in this region to predict the rapid flow variation properly. The same process is also used in the region immediately behind the front of the exhausting rarefaction wave. Note that in Fig. 8, the characteristics are not shown in this region. To save the computational cost, which increases with the number of characteristics, we stopped the calculation at the thick dotted C_+ characteristic named A-A' and introduced new C_- characteristics from the dividing points equally spaced on A-A'.

As already mentioned, when using the method of characteristics, the grid is described by the waves, or characteristics, themselves. Consequently, the grid cannot be predefined, and its resolution largely depends on the number of discrete segments on the detonation wave, N, and the initial Taylor expansion fan, M. The flow solution converges as N and M increase. We determine that N=M=300, which is large enough for the $I_{\text{end-wall}}$ calculated from the solution to be in the range of 0.02% of the convergent value.

To compare the present model with the experimental measurements, we calculate the pressure field with the following equation:

$$p = p_{\mathrm{CJ}} A^{\frac{2\Gamma}{\Gamma-1}} \exp\left\{-\Gamma\left(S - S_{\mathrm{CJ}}\right)\right\} \tag{30}$$

This equation is derived from the energy equation and the ideal-gas equation, that is, $p=\rho RT$. In addition to the pressure field, we calculate the net specific impulse that the DT obtains during the single detonation cycle by placing a control volume whose surface surrounds the fluid inside the DT, as shown in Fig. 10, and considering the conservation of momentum. Naming the closed-end surface "1," the open-end surface "2," and the side-wall surface "side," we derive the following momentum equation in the axial direction:

$$\frac{\partial}{\partial t}\int_1^2 \rho u A \mathrm{d}x + \left(\rho_2 A_2 {u_2}^2 - \rho_1 A_1 {u_1}^2\right) = \left(p_1 - p_0\right)A_1 - \left(p_2 - p_0\right)A_2 - \oiint_{\mathrm{side}} \tau_{\mathrm{w}} \mathrm{d}s \tag{31}$$

where τ_{w} is the shear stress on the surface "side," given as follows with the frictional coefficient C_{f}:

$$\tau_{\mathrm{w}} = \frac{1}{2} C_{\mathrm{f}} \rho u |u| \tag{32}$$

The left-hand side of Eq. (31) consists of two terms, the contribution from non-stationary changes inside the DT and the contribution from the flux of momentum into the DT through the surfaces "1" and "2." The right-hand side is the force due to the pressures on the surfaces "1" and "2" and the shear stress on the surface "side." Solving Eq. (31) for the pressure at the thrust wall and integrating it with respect to time until $t=t_{\mathrm{cyc}}$, we have the following equation:

$$\int_0^{t_{\mathrm{cyc}}} \left(p_1 - p_0\right)A_1 \mathrm{d}t = \int_0^{t_{\mathrm{cyc}}} \left[\frac{\partial}{\partial t}\int_1^2 \rho u A \mathrm{d}x + \rho_2 A_2 {u_2}^2 + \left(p_2 - p_0\right)A_2 + \oiint_{\mathrm{side}} \tau_{\mathrm{w}} \mathrm{d}s\right] \mathrm{d}t \tag{33}$$

From Eq. (5), we have

$$I_{\text{net-thrust}} - I_{\text{end-wall}} = -\int_0^{t_{\mathrm{cyc}}} \left(\oiint_{\mathrm{side}} \tau_{\mathrm{w}} \mathrm{d}s\right) \mathrm{d}t \tag{34}$$

Substituting Eqs. (1) and (34) into Eq. (33), we can obtain the net specific impulse of the DT, as follows:

$$I_{\text{net-thrust}} = \int_0^{t_{\mathrm{cyc}}} \left[\frac{\partial}{\partial t}\int_1^2 \rho u A \mathrm{d}x + \rho_2 A_2 {u_2}^2 + \left(p_2 - p_0\right)A_2\right] \mathrm{d}t \tag{35}$$

IV. Comparison of Experimental Results and the Model

A total of 60 single-shot experiments were conducted for the 7 experimental conditions described previously. Figure 11(a) and (b) show the distribution of $I_{sp,end\text{-}wall}$ and $I_{sp,net\text{-}thrust}$, respectively, for each shot carried out in this series of experiments, except for shot condition LT. In each vertical line, the experimental results obtained in each shot are shown, that is, three $I_{sp,end\text{-}wall}$ (CH1-CH3) in Fig. 11(a) and two $I_{sp,net\text{-}thrust}$ (Video Camera and Laser) in Fig. 11(b) are plotted. The results are sorted by shot condition and arranged from P1 on the far left to N3 on the far right. For reference, the ideal specific impulse, I_{isen}, is shown with a dotted line.

As shown in Fig. 11(a), the experimental value of $I_{sp,end\text{-}wall}$ is widely dispersed for every shot. To eliminate doubtful results from the three $I_{sp,end\text{-}wall}$ (CH1-CH3) values, we determine the representative value for each shot as follows. First, we pick out the two values that are the closest to each other among three values, and then we determine the representative value of the shot as the average of the two values. Figure 11(c) shows the representative values determined for each shot. Regarding $I_{sp,net\text{-}thrust}$, since there is little difference between two kinds of $I_{sp,net\text{-}thrust}$, the value with the laser displacement gauge is adopted as the representative for the present.

Averaging these representatives for each of the experimental conditions, we determine the most probable value of the condition for $I_{sp,thrust\text{-}wall}$ and $I_{sp,net\text{-}thrust}$. Among pressure histories for each condition, we single out the history whose integration is the closest to the most probable value of $I_{end\text{-}wall}$ as the representative history. The pressure history is fast-Fourier-transform filtered to eliminate the periodic pressure oscillations, which originate from the pressure wave propagating in the radial direction [26]. As the cut-off frequency we use the same-order value as the vibrational frequency of this pressure oscillation that is predicted with the tube diameter and sonic velocity of the burned gas.

Figures 12 and 13 show the pressure histories of the polished tubes and normal tubes. We take time as the horizontal axis whose origin is the time of ignition. As the vertical axis, we take the non-dimensional pressure, in which the so-called plateau pressure [12], p_{pl}, is used as a reference, as follows:

$$p_{pl} = \frac{\gamma}{2\Gamma}\left(\frac{\Gamma+1}{2\Gamma}\right)^{\frac{\Gamma+1}{\Gamma-1}} {M_{CJ}}^2 p_1 \tag{36}$$

In this way the pressure immediately after ignition becomes unity for all experiments, and we can compensate for the differences in experimental conditions such as ambient temperature and initial pressure. As shown in Figs. 12

and 13, the pressure at the closed end declines gradually from the plateau pressure, and after that, strong expansion is caused when the exhausting rarefaction wave from the open end reaches the closed end. Due to this strong expansion, the pressure at the closed end falls below the ambient pressure, but it recovers to values very close to ambient as a result of the arrival of the weak shock wave (e. g., after 6 ms in the case of P1 in Fig. 12). The origin of this shock wave is at the exit of the tube. Once the pressure at the exit reaches the ambient level, the expansion waves are reflected as compression waves, and they quickly coalesce into the weak shock wave [38]. In this sequence of typical pressure variation, we focus on the pressure gradient in the region before the exhausting rarefaction wave arrives from the open end. This region is called the "plateau region," since if the flow is assumed to be isentropic, the pressure in this region becomes flat as its name suggests. In the actual flow, however, the pressure at the closed end attenuates, because the expansion wave is generated at the side wall of the tube by the wall losses due to heat transfer and friction, and it reaches the closed end as the family of C_- characteristics from the detonation wave, as shown in Fig. 8. Thus the pressure gradient at the plateau region is associated with the wall losses. In the case of the polished tube in Fig. 12, the pressure gradients for three different tube lengths are in good agreement with each other at the plateau region. On the other hand, in the case of the normal tube in Fig. 13, although the pressure gradient at the plateau region of N1 is in good agreement with N2 and N3, the waveform of N3 shifts upward a little after the end of the plateau of N1 and deviates from the waveform of N2. This is because small pressure perturbations are caused continuously when the flow passes through the irregularity at the connecting point of the coupled two tubes at N3. They propagate to the closed end and increase the pressure there. In addition, the little peaks at the plateau region of N2 and N3 are the influence of perturbations caused when the detonation wave propagates past the pressure taps on the side wall.

Figure 14 shows the pressure histories of a polished tube and a normal tube of L/D=49, and Fig. 15 and 16 are the pressure histories in the cases of L/D=103 and L/D=151, respecitvely. In these figures, we cannot recognize a significant difference greater than the margin of error between the pressure histories of the polished and normal tubes, because the surface roughness of both tubes is categorized as so-called "hydraulically smooth," where the amount of roughness is so small that all protrusions are contained within the laminar sub-layer and the friction coefficient, C_f, is not dependent on the surface roughness but is a function of only the Reynolds number [39]. To reveal the relationship between the surface roughness of the inner wall and the performance of the DT, we need to

perform additional experimental investigation using tubes with “completely rough” surfaces in which all protrusions reach outside the laminar sub-layer.

The experimental and calculated pressure histories with various tube lengths corresponding to P1, P2, P3, and LT are shown in Figs. 17 to 20, respectively. The experimental pressure at the plateau region starts to decline with a steeper gradient than the simulation after the ignition, and it decays, showing a convex downward curve with a larger curvature than the calculation, which is more apparent in cases with longer tubes, such as in Fig. 20. This disagreement in waveform shape indicates the possibilities of other wall loss mechanisms in the actual flow field than the heat transfer and friction considered in the present model. Owens and Hanson [27] showed with experiments and a one-dimensional model that in addition to heat transfer and friction, water condensation at the cold wall whose surface temperature is below the saturation temperature significantly attenuates the pressure in the tube. They predicted that as the condensate film growth rate decreases with the passage of time, the rate of pressure decay in the plateau region gradually diminishes. Since the same trend can be observed in the present experiments, one of the reasons for the discrepancy between the experimental and calculated pressure in the present study may be the effect of condensation.

In addition to water condensation, conductive heat transfer at the stagnant gas region behind the detonation wave may be one of the reasons for the difference between the pressure profiles of the simulations and the experiments. In this region, the present model predicts heat flux to be zero, because the heat transfer coefficient, C_h, becomes zero when u=0, as shown in Eq. (12). However, in the actual flow the heat flux is not zero, since heat is conducted from the high-temperature gas to the cold tube wall. This means that the present model under-predicts the heat flux at the stagnant gas region. In addition, heat transfer causes a temperature increase at the inner wall, which is assumed to be constant in the model, and as a result of this, heat transfer is considered to be suppressed relative to the model. This effect emerges notably at the stagnant gas region because, as shown in Fig. 8, the C_- characteristics that arrive at the end wall later have taken longer to pass through that region, and consequently, the pressure profile in that region becomes a convex downward curve. Owens and Hanson [27] also confirmed the presence of constant heat flux due to conduction in the stagnation gas region.

In addition to the plateau region, the experimental and numerical profiles are different in the point that the experimental pressure profiles show the arrival of a weak shock wave at the thrust wall, while the numerical calculation does not. This is a consequence of the imperfect boundary condition at the tube exit in the current

simulation. We assume that the flow at the exit of the tube is sonic outflow for the entire simulation. However, in fact, the flow there changes from outflow to inflow depending on whether the pressure at the exit is above the ambient level or not. The weak shock wave is formed exactly at the time when the direction of the flow changes, which is named τ_{ws} in non-dimensional form. It is illustrated on the ξ-τ plane of Fig. 8. With the dashed-dotted line, the C_- characteristic from ξ=1, τ=τ_{ws} is shown, which corresponds to the path of the weak shock. The influence due to differences in the exit boundary conditions cannot be recognized on the pressure profiles until the arrival of the weak shock, and we consider the same to be true in other locations all over the tube.

Figure 21 shows a comparison of the pressure profiles measured at the closed end and at three locations on the side wall of the DT of N3 with the simulation. These profiles are shifted up by 1.5 MPa for clarity, and the locations of the pressure transducers are shown in x/L. As shown in the figure, good agreement of the simulation with the experiment is confirmed not only at the closed-end wall but also at the other locations.

Next, we examine the process of generating the specific impulse, applying the conservation of momentum to the flow inside the control volume described previously. Replacing the upper limit of the integral to an arbitrarily chosen time and naming every term ① to ⑤ as follows, the history of every term can be obtained from the calculation results with the method of characteristics:

$$\underset{①}{\int_0^t (p_1 - p_0) A_1 \mathrm{d}t} = \int_0^t \left[\underset{②}{\frac{\partial}{\partial t} \int_1^2 \rho u A \mathrm{d}x} + \underset{③}{\rho_2 A_2 {u_2}^2} + \underset{④}{(p_2 - p_0) A_2} + \underset{⑤}{\iint_{\text{side}} \tau \mathrm{d}s} \right] \mathrm{d}t \tag{37}$$

Figure 22 shows a comparison of the left-hand side of Eq. (37) with the right-hand side, both of which are calculated using the experimental condition P3. The colored areas are a pile of the terms ②+③+④+⑤, and with the dotted line, a profile of $I_{sp,isen}$ is shown for reference, and hence area ⑥ represents $I_{sp,pressure\text{-}deficit}$. We take the non-dimensional time τ=t/t_{CJ} as the horizontal axis, where t_{CJ} is the time when the detonation wave arrives at the open end of the tube. As shown in the figure, the good agreement of the right-hand side with the left-hand side is confirmed.

In term ② of Eq. (37), as the integral and differential operators are canceled, this term can be interpreted as the gross momentum of the gases flowing inside the control volume. Consequently, focusing on the variation of area ②, we can understand the behavior of the flow inside the tube in gross. To promote understanding in the following discussion, we indicated in Fig. 22 several characteristic times that were shown in Fig. 8 for ease in comparison with

it. In the range of $0 \le \tau \le \tau_{CJ}=1$ in Fig. 22, area ② increases rapidly, because the combustible mixture at rest ahead of the detonation wave is accelerated to a sonic flow continuously by the propagating of the detonation wave. At $\tau=1$, the gross momentum begins to decrease, because when $\tau=1$, the detonation wave reaches the exit and the high-speed product starts to be exhausted out of the tube. However, the effect of decreasing the momentum gradually weakens as time elapses, because the exhausting rarefaction wave propagating into the tube accelerates the flow and increases term ②. Before time $\tau=\tau_t$ when the rear end of the Taylor expansion wave reaches the tube exit, which is illustrated in the Fig. 8, the effect of increasing surpasses the effect of decreasing and area ② shifts to increasing. After a while, area ② shifts to decreasing again, because the exhausting rarefaction wave arrives at the closed end of the tube at $\tau \approx \tau^*$ and the effect of acceleration fails. Figure 22 shows the range of $0 \le \tau \le \tau_{cyc}$. At $\tau=\tau_{cyc}$, the gross momentum becomes very small but not zero, which indicates that the flow is not completely at rest in the DT. Terms ③ and ④ are the integral of the momentum flux and pressure at the open end of the tube, respectively. They appear to start to increase on behalf of term ② at time $\tau=1$ when the detonation wave arrives at the open end.

Figure 23 shows the history of force, which is the integral of shear stress with respect to the side wall surface of the DT. Since shear stress is proportional to the square of flow velocity, as shown in Eq. (35), the waveform in Fig. 23 shows a similar tendency to that of area ② in Fig. 22, which is proportional to the flow velocity. The integral of the force in Fig. 18 with respect to time becomes term ⑤ in Fig. 17. Subtracting term ⑤ from term ①, ②+③+④ yields the history of $I_{sp,net\text{-}thrust}$, as given in Eq. (35).

Table 2 summarizes the experimental results for the most probable values of I_{sp} obtained in all shot conditions except LT. In this table, the I_{sp} efficiencies $\eta_{end\text{-}wall}$ and $\eta_{net\text{-}thrust}$ are calculated by taking the ratio of the measured I_{sp} to $I_{sp,isen}$ from the ideal theory, and this reveals how much potential impulse can be exploited by the practical PDE. For example, focusing on the results of shot condition P3, we see that the impulse acting on the DT drops to 78% of the ideal impulse, because 22% of $I_{sp,isen}$ is lost as the pressure deficit due to heat transfer and friction. In addition, 14% of $I_{sp,isen}$ is lost from $I_{sp,end\text{-}wall}$ due to shear stress on the side wall, and then the DT obtains 64% of the ideal impulse as the momentum. This shows that the shear stress has a dominant influence on the performance of the DT in shot condition P3. The same results are obtained in shot conditions P2, N2, and N3, in which the ratio of $I_{sp,side\text{-}wall}$ to $I_{sp,pressure\text{-}deficit}$ ranges from 0.63 to 0.78, as shown in the far right column of Table 2. At P1 and N1, on the other hand, the losses due to shear stress becomes almost zero or below zero. The probable reason for the negative losses due to shear stress is that the additional thrust acts on the lip of the exit of the DT due to overpressure after the

diffraction of the detonation wave, and it contributes to shifting up $I_{\text{net-thrust}}$ and hence shifting down $I_{\text{side-wall}}$. Cooper et al. [40] conducted experiments with a flat plate attached to the open end of a DT, which extended radially in the direction perpendicular to the tube axis. Although they reached no conclusion about the influence of the flat plate on the performance, they observed that the flat plate extension increased a specific impulse by 5% in the case of the stoichiometric ethylene-oxygen detonation wave, compared with no extension at the open end. However, even if the contribution of the additional thrust is excluded, the influence of the shear stress is remarkably small in shot conditions P1 and N1 relative to the others. The absence of skin friction on the side wall was also observed by the experimental measurements of specific impulse by Harris et al. [18] with the DT of L/D=49.5. However, at the moment, the detailed mechanism of low shear stress in the small L/D remains an open issue.

Figure 24 shows the experimental results in Table 2 with symbols, taking L/D as the horizontal axis, and the figure also shows the variation of computed I_{sp} with L/D. Similar to Fig. 22, the colored areas are a pile of the terms ②+③+④+⑤. Here, $I_{\text{sp,isen}}$ and $I_{\text{sp,pressure-deficit}}$ are shown with a dotted line and as area ⑥, respectively. For the end time of these integrals, we use t_{cyc}, which is the time when the pressure at the closed end of the tube first decays to the ambient level. The integral range $0 \le t \le t_{\text{cyc}}$ includes the range after the passage of the weak shock wave, as shown in Fig. 8, and we need to consider the influence of the choked outflow condition again. However, because this range is small compared to the integral range, and moreover the flow state of the inflow at the exit is considered to be small compared to the outflow, the influence of the choked outflow condition can be considered negligible. The present model predicts the measurement values very well, especially in the range of $103 \le L/D \le 151$. However, closer comparison clarifies a little discrepancy between the experimental results of $I_{\text{sp,end-wall}}$ and the computation. One cause of the discrepancy is the effect of water condensation, as mentioned previously. Owens and Hanson [27] quantified the magnitude of the effect of water condensation on the specific impulse indirectly by subtracting the measurement results of the pressure-based I_{sp} from the simulations that considered the effect of heat transfer and friction but not water condensation. They showed that more than half of $I_{\text{sp,pressure-deficit}}$ is caused by the effect of water condensation with the DT of an arbitrary diameter and T_{w}=298 K. However, due to the complexity of the mechanism of water condensation, it is still difficult to directly simulate the magnitude of its effect on the losses of the specific impulse. We need to consider how to incorporate the effect of water condensation into our model through an experimental parametric analysis of its effect.

In addition to the good agreement of the current results for simulations with the experiments, we confirmed that the present prediction for $I_{sp,net\text{-}thrust}$ agrees with the ballistic pendulum measurements obtained by earlier researchers within ±9.3% accuracy in hydrogen-oxygen mixtures [16, 19] and ±3.3% accuracy in propane-oxygen mixtures [16, 18, 40] in the range of $L/D \leq 60$. We obtained accuracy similar to that reached by Radulescu and Hanson [26] in their model and the experimental results we referred.

In the final part of the present study, we discuss an optimal design of PDE systems. As shown in Fig. 24, frictional losses are negligible in the case of L/D=49 but friction significantly reduces the performance of the DT of L/D=103 and 151. From this result, $L/D \approx 50$ would seem to be the best aspect ratio for a PDE. Moreover, the addition of a diverging nozzle would be effective for further increasing the performance of this engine, because it is known from Ref. 30 that the extension of the engine with the diverging nozzle has the effect of increasing the net I_{sp} in spite of wall losses from heat transfer and friction, which is in contrast to the lengthening of the straight tube. In the present study, we consider only the case of the single-pulse detonation tube. For multi-cycle operation, as would be encountered in PDE applications, we should consider the influence of the wall temperatures, which will be much higher than T_w=298 K due to the long duration of the hot detonation products. According to Ref. 27, since the hot wall suppresses water condensation, the pressure-based I_{sp} increases as the wall temperature approaches the saturation temperature of water vapor. However, we did not determine how frictional losses change as the effect of water condensation is reduced, and therefore, further investigation is needed to determine the optimal wall temperatures to exploit the performance of the PDE.

V. Conclusion

Single-shot DT experiments were carried out with various L/D in the range of 50 to 250. The measurements of I_{sp} revealed how much potential impulse can be exploited by the practical PDE. As a result of the I_{sp} losses due to various wall loss mechanisms, the DT obtained 89%, 70%, and 64% of the ideal impulse as the momentum for a polished tube of L/D=49, 103, and 151, respectively. The losses due to skin friction on the side wall were also evaluated. Although the shear stress had a dominant influence on the performance of the DT of L/D=103 and 151, it was found to become remarkably small for L/D=49 relative to the longer tubes.

These experimental results were compared with the simple one-dimensional gas-dynamic model considering only heat transfer and friction as wall loss mechanisms, and thus they validate only this most simplified model.

Although small discrepancies between the model and experiments were observed, which were considered to be due to the influence of condensation and heat conduction, the present model predicted the experimental results very well, especially in the range of $103 \leq L/D \leq 151$.

Acknowledgement

This work was subsidized by the Ministry of Education, Culture, Sports, Science and Technology, a Grant-in-Aid for Scientific Research (A), No. 20241040; a Grant-in-Aid for Scientific Research (B), No. 21360411; and the Research Grant Program from the Institute of Space and Astronautical Science, the Japan Aerospace Exploration Agency. The authors wish to thank R. Kojima, S. Fukuda, and A. Kojima from the University of Tsukuba for launching the initial experimental apparatuses, for help in obtaining experimental data, and for supporting the experiments as a technical staff person, respectively.

References

[1] Nicholls, J. A., Wilkinson, H. R., and Morrison, R. B., "Intermittent Detonation as a Thrust-Producing Mechanism," *Jet Propulsion*, Vol. 27, No. 5, 1957, pp. 534–541.

[2] Bussing, T. R. A., and Pappas, G., "Pulse Detonation Engine Theory and Concepts," *Developments in High-Speed-Vehicle Propulsion Systems: Progress in Astronautics and Aeronautics*, Vol. 165, AIAA, Reston, VA, 1996, pp. 421–472.

[3] Kailasanath, K., "Review of Propulsion Applications of Detonation Waves," *AIAA Journal*, Vol. 38, No. 9, 2000, pp. 1698–1708.
doi:10.2514/2.1156

[4] Kailasanath, K., "Recent Developments in the Research on Pulse Detonation Engines," *AIAA Journal*, Vol. 41, No. 2, 2003, pp. 145–159.
doi:10.2514/2.1933

[5] Kasahara, J., Hasegawa, A., Nemoto, T., Yamaguchi, H., Yajima, T., and Kojima, T., "Performance Validation of a Single-Tube Pulse Detonation Rocket System," *Journal of Propulsion and Power*, Vol. 25, No. 1, 2009, pp. 173–180.
doi:10.2514/1.37924

[6] Wu, Y. H., Ma, F. H., and Yang, V., "System Performance and Thermodynamic Cycle Analysis of Airbreathing Pulse Detonation Engines," *Journal of Propulsion and Power*, Vol. 19, No. 4, 2003, pp. 556–567.
doi: 10.2514/2.6166

[7] Sato, S., Matsuo, A., Endo, T., and Kasahara, J., "Numerical Studies on Specific Impulse of Partially Filled Pulse Detonation Rocket Engines," *Journal of Propulsion and Power*, Vol. 22, No. 1, 2006, pp. 64–69.
doi:10.2514/1.9514

[8] Endo, T., Yatsufusa, T., Taki, S., Matsuo, A., Inaba, K., and Kasahara, J., "Homogeneous-Dilution Model of Partially-Fueled Simplified Pulse Detonation Engines," *Journal of Propulsion and Power*, Vol. 23, No. 5, 2007, pp. 1033–1041.
doi:10.2514/1.21223

[9] Kasahara, J., Liang, Z., Browne, S. T., and Shepherd, J. E., "Impulse Generation by an Open Shock Tube," *AIAA Journal*, Vol. 46, No. 7, July 2008, pp. 1593–1603.
doi:10.2514/1.27467

[10] Kasahara, J., Hirano, M., Matsuo, A., Daimon, Y., and Endo, T., "Thrust Measurement of a Multicycle Partially Filled Pulse Detonation Rocket Engine," *Journal of Propulsion and Power*, Vol. 25, No. 6, 2009, pp. 1281–1290.
doi: 10.2514/1.42224

[11] Morris, C. I., "Numerical Modeling of Single-Pulse Gasdynamics and Performance of Pulse Detonation Rocket Engines," *Journal of Propulsion and Power*, Vol. 21, No. 3, 2005, pp. 527–538.
doi:10.2514/1.7875

[12] Endo, T., and Fujiwara, T., "A Simplified Analysis on a Pulse Detonation Engine Model," *Transactions of the Japan Society for Aeronautical and Space Sciences*, Vol. 44, No. 146, 2002, pp. 217–222.
doi:10.2322/tjsass.44.217

[13] Endo, T., Kasahara, J., Matsuo, A., Inaba, K., Sato, S., and Fujiwara, T., "Pressure History at the Thrust Wall of a Simplified Pulse Detonation Engine," *AIAA Journal*, Vol. 42, No. 9, 2004, pp. 1921–1929.
doi:10.2514/1.976

[14] Wintenberger, E., Austin, J. M., Cooper, M., Jackson, S., and Shepherd, J. E., "Analytical Model for the Impulse of Single-Cycle Pulse Detonation Tube," *Journal of Propulsion and Power*, Vol. 19, No. 1, 2003, pp. 22–38.
doi:10.2514/2.6099

[15] Takeuchi, S., Doi, N., Kasahara, J., Murayama, M., and Matsuo, A., "Net Impulse Measurements of Pulse Detonation Tube by Using Fuel-Air Mixture," *AIAA Paper*, 2010-148, January 2010.

[16] Laviolette, J. P., Kiyanda, C. B., and Higgins, A. J., "The Effect of Friction and Heat Transfer on Impulse in a Detonation Tube," Canadian Section of Combustion Institute, May 2002.

[17] Kasahara, J., Tanahashi, Y., Numata, T., Matsuo, A., and Endo, T., "Experimental Studies on *L/D* Ratio and Heat Transfer in Pulse Detonation Engines," 19th International Colloquium on the Dynamics of Explosions and Reactive Systems, Paper 65, July–Aug. 2003 (on CD-ROM).

[18] Harris, P. O., Farinaccio, R., Stowe, R. A., Higgins, A. J., Thibault, P. A., and Laviolette, J. P., "The Effect of DDT Distance on Impulse in a Detonation Tube," *AIAA Paper* 2001-3467, July 2001.

[19] Kiyanda, C. B., Tanguay, V., Higgins, A. J., and Lee, J. H. S., "Effect of Transient Gasdynamic Processes on the Impulse in Pulse Detonation Engines," *Journal of Propulsion and Power*, Vol. 18, No. 5, 2002, pp. 1124–1126.
doi: 10.2514/2.6045

[20] Sichel, M., and David, T. S., "Transfer Behind Detonations in H2-O2 Mixtures," *AIAA Journal*, Vol. 4, No. 6, 1966, pp. 1089, 1090.

[21] Mirels, H., "The Wall Boundary Layer behind a Moving Shock Wave," *Boundary Layer Research*, edited by H. Görtler, Freiburg Symposium, 1957, pp. 283-293.

[22] Hartunian, R. A., Russo, A. L., and Marrone, P. V., "Boundary Layer Transition and Heat Transfer in Shock Tubes," *Journal of Aerospace Science*, Vol. 27, 1960, pp. 587-94

[23] Skinner, J. H., Jr., "Friction and Heat-Transfer Effects on the Nonsteady Flow Behind a Detonation," *AIAA Journal*, Vol. 5, No. 11, 1967, pp. 2069–2071.
doi: 10.2514/3.4374

[24] Edwards, D. H., Brown, D. R., Hooper, G., and Jones, A. T., "The Influence of Wall Heat Transfer on the Expansion Following a C-J Detonation Wave," *Journal of Physics D: Applied Physics*, Vol. 3, No. 3, 1970, pp. 365–376.
doi:10.1088/0022-3727/3/3/317

[25] Kojima, R., "Study on Wall Thrust Losses in a Pulse Detonation Engine" Master Thesis, Dept. of Engineering Mechanics and Energy, Univ. of Tsukuba, Ibaraki, Japan, 2007

[26] Radulescu, M. I., and Hanson, R. K., "Effect of Heat Loss on Pulse-Detonation-Engine Flow Fields and Performance," *Journal of Propulsion and Power*, Vol. 21, No. 2, 2005, pp. 274–285.
doi:10.2514/1.10286

[27] Owens, Z. C., and Hanson, R. K., "The Influence of Wall Heat Transfer, Friction and Condensation on Detonation Tube Performance," *Combustion, Science and Technology*, Vol. 182, No. 8, 2010, pp. 1104-1140.
doi: 10.1080/00102200903485202

[28] Owens, Z.C., Mattison, D.W., Barbour, E.A., Morris, C.I. and Hanson, R.K., "Flowfield Characterization and Simulation Validation of Multiple-Geometry PDEs using Cesium-Based Velocimetry." *Proceedings of the Combustion Institute*, 30, 2005, pp. 2791-2798.
doi:10.1016/j.proci.2004.08.050

[29] Mattison D.W, Oehlschlaeger M.A., Morris C.I., Owens Z.C., Barbour E.A., Jeffries J.B. and Hanson R.K., "Evaluation of Pulse Detonation Engine Modeling using Laser-Based Temperature and OH Concentration Measurements," *Proceedings of the Combustion Institute*, 30, 2005, pp. 2879-2807.
doi:10.1016/j.proci.2004.08.026

[30] Barbour, E. A., and Hanson, R.K., "Chemical Nonequilibrium, Heat Transfer, and Friction in a Detonation Tube with Nozzles," *Journal of Propulsion and Power*, Vol. 26, No. 2, 2010, pp. 230–239.
doi: 10.2514/1.44814

[31] Kawane, K., Shimada, S., Kasahara, J., and Matsuo, A., "The Influence of Heat-Transfer and Friction on the Impulse of a Single-Cycle Pulse Detonation Tube," 22nd International Colloquium on the Dynamics of Explosions and Reactive Systems, Paper 163, July 2009 (on CD-ROM).

[32] Radulescu, M. I., and Hanson, R. K., Comment on "Analytical Model for the Impulse of Single-Cycle Pulse Detonation Tube," *Journal of Propulsion and Power*, Vol. 20, No. 5, 2004, pp. 956–959.
doi: 10.2514/1.7876

[33] Radulescu, M. I., Morris, C. I., and Hanson, R. K., "The Effect of Wall Heat Loss on the Flow Fields in a Pulse-Detonation Wave Engine," *AIAA Paper* 2004-1124, Jan. 2004.

[34] Holman, J. P., *Heat Transfer*, 9th ed., McGraw-Hill, Inc., New York, Chap. 5, pp. 230-232.

[35] Penner, S. S., *Chemistry Problems in Jet Propulsion*, Pergamon Press, New York, 1957, Chap. XIX, p. 249.

[36] Foa, J. V., *Elements of Flight Propulsion*, Wiley, New York, 1960, p. 90.

[37] Tanaka, K., "Thermochemical Database of Gases and Condensed Materials: AISTJAN,"
http://riodb.ibase.aist.go.jp/ChemThxrm/aistjan.html

[38] Guzik, S. M., Harris, P. G., and De Champlain, A., "An Investigation of Pulse Detonation Engine Configurations Using the Method of Characteristics," *AIAA Paper* 2002-4066, July 2002.

[39] Schlichting, H., *Boundary-Layer Theory*, McGraw–Hill, New York, 1968, pp. 578-580.

[40] Cooper, M., Jackson, S., Austin, J., Wintenberger, E., and Shepherd, J. E., "Direct Experimental Impulse Measurements for Detonations and Deflagrations," *Journal of Propulsion and Power*, Vol. 18, No. 5, 2002, pp. 1033–1041.
doi:10.2514/2.6052

Table 1 Experimental conditions

Shot Condition	*L* [mm]	*D* [mm]	*L/D*	R_a/D (Surface Finish)	Ballistic Pendulum	Number of Shots
P1	1237	25.5	49	5.00×10^{-5} (Polished)	hanging	8
P2	2635	25.5	103	5.00×10^{-5} (Polished)	hanging	6
P3 (=P1+P2)	3841	25.5	151	5.00×10^{-5} (Polished)	hanging	11
N1	1237	25.5	49	1.96×10^{-4} (Normal)	hanging	14
N2	2635	25.5	103	1.96×10^{-4} (Normal)	hanging	8
N3 (=N1+N2)	3841	25.5	151	1.96×10^{-4} (Normal)	hanging	8
LT (=P1+P2+N2)	6446	25.5	253	(Polished+Normal)	fixed	5

Table 2 Experimental Results

Shot Condition	$I_{sp,isen}$ [sec]	$I_{sp,end\text{-}wall}$ [sec]	I_{sp} efficiency $\eta_{end\text{-}wall}$	$-I_{sp,pressure\text{-}deficit}$ [sec]	$I_{sp,net\text{-}thrust}$ [sec]	I_{sp} efficiency $\eta_{net\text{-}thrust}$	$-I_{sp,side\text{-}wall}$ [sec]	ratio of I_{sp} losses
	(a)	(b)	(b) / (a)	(c) = (a) - (b)	(d)	(d) / (a)	(e) = (b) - (d)	(e) / (c)
P1	167.7	149.1 ± 2.9	0.89	18.6	148.5 ± 3.0	0.89	0.6	0.03
P2	167.7	137.8 ± 2.6	0.82	29.9	116.3 ± 3.0	0.69	21.5	0.72
P3 (=P1+P2)	167.7	131.4 ± 2.3	0.78	36.3	107.1 ± 2.1	0.64	24.3	0.67
N1	167.7	149.1 ± 2.9	0.89	18.6	154.0 ± 3.5	0.92	-4.9	-0.26
N2	167.7	138.6 ± 2.7	0.83	29.1	120.3 ± 3.4	0.72	18.3	0.63
N3 (=N1+N2)	167.7	132.3 ± 2.5	0.79	35.4	104.8 ± 2.6	0.62	27.5	0.78

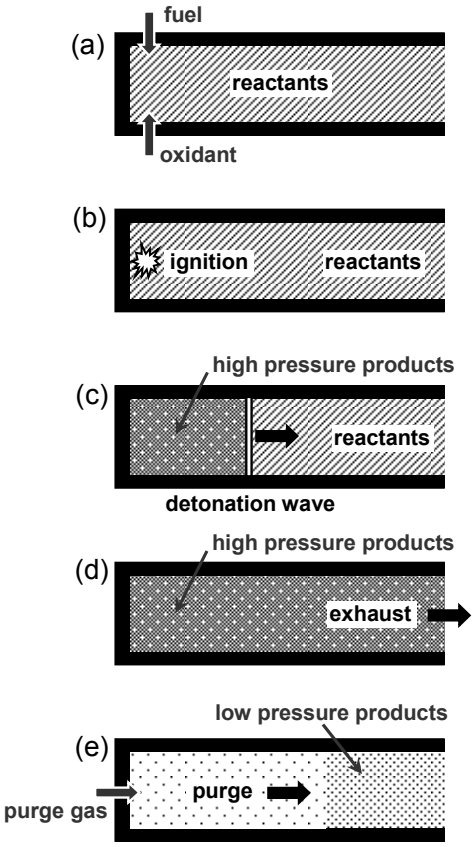

Fig. 1 The general PDE cycle.

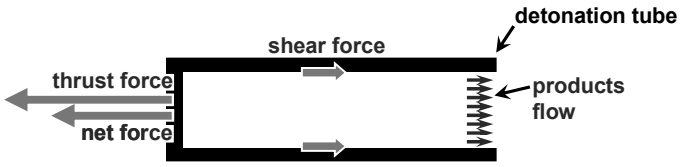

Fig. 2 Schematic diagram of the forces on the detonation tube.

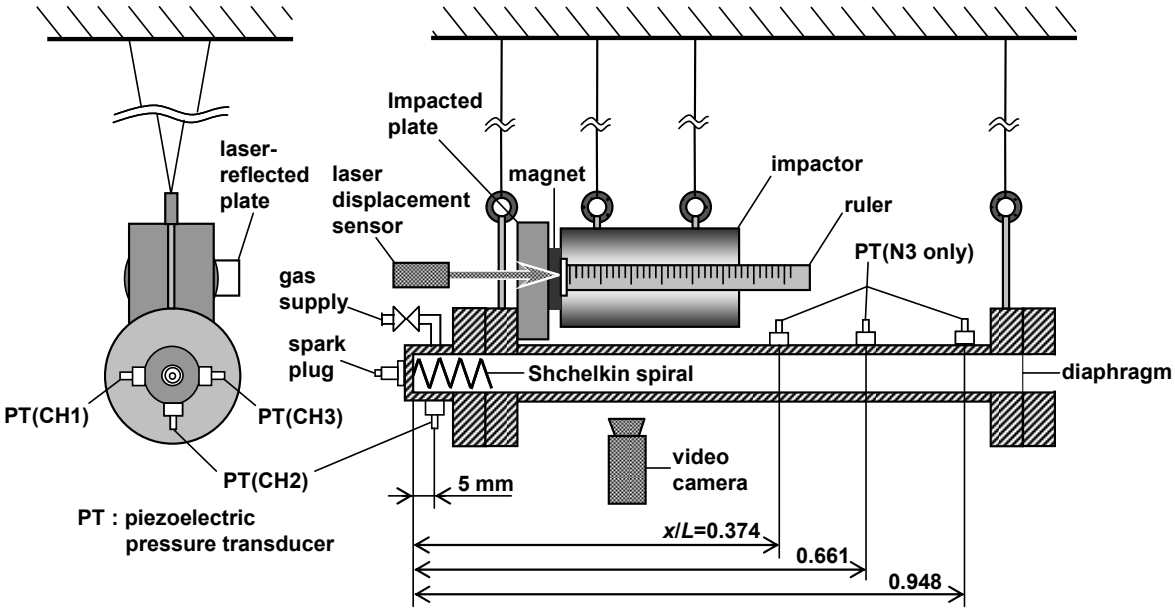

Fig. 3 Schematic diagram of the experimental device.

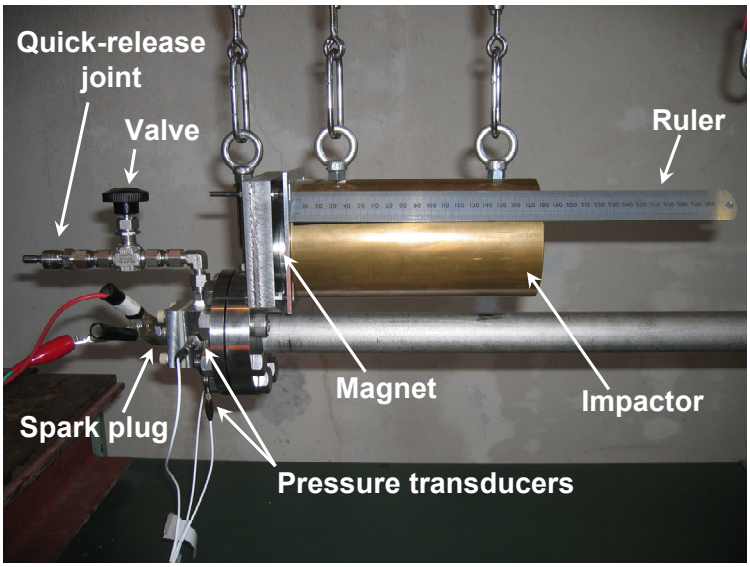

Fig. 4 Photograph of the experimental device.

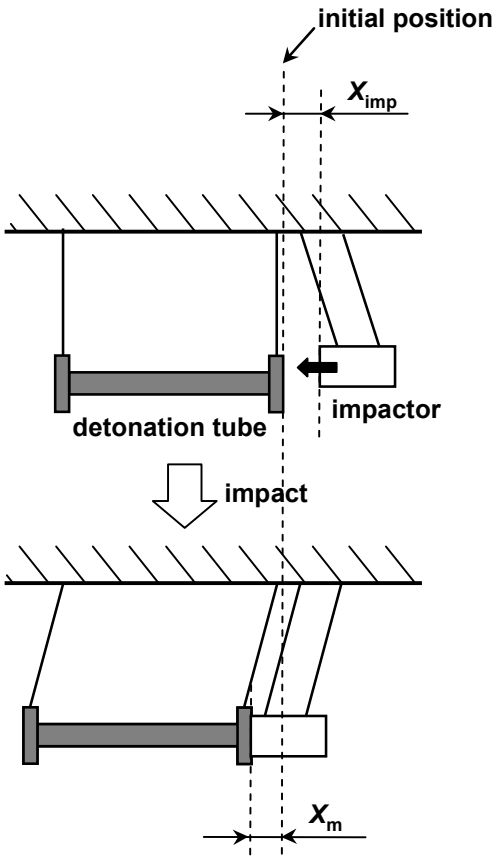

Fig. 5 Schematic diagram of the impactor calibration method.

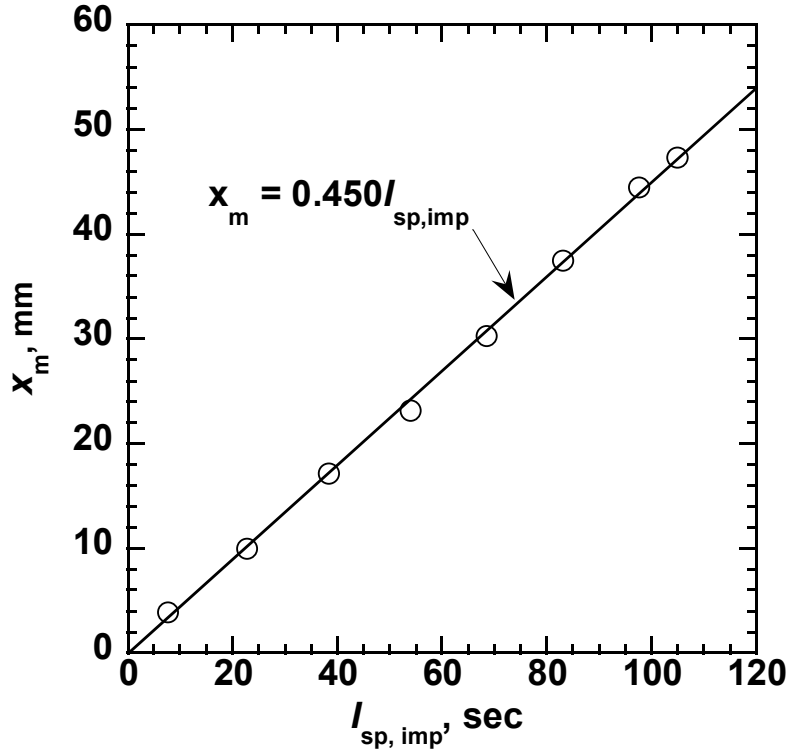

Fig. 6 Linear relationship between maximum horizontal displacement and corresponding specific impulse of the impactor in the case of P3.

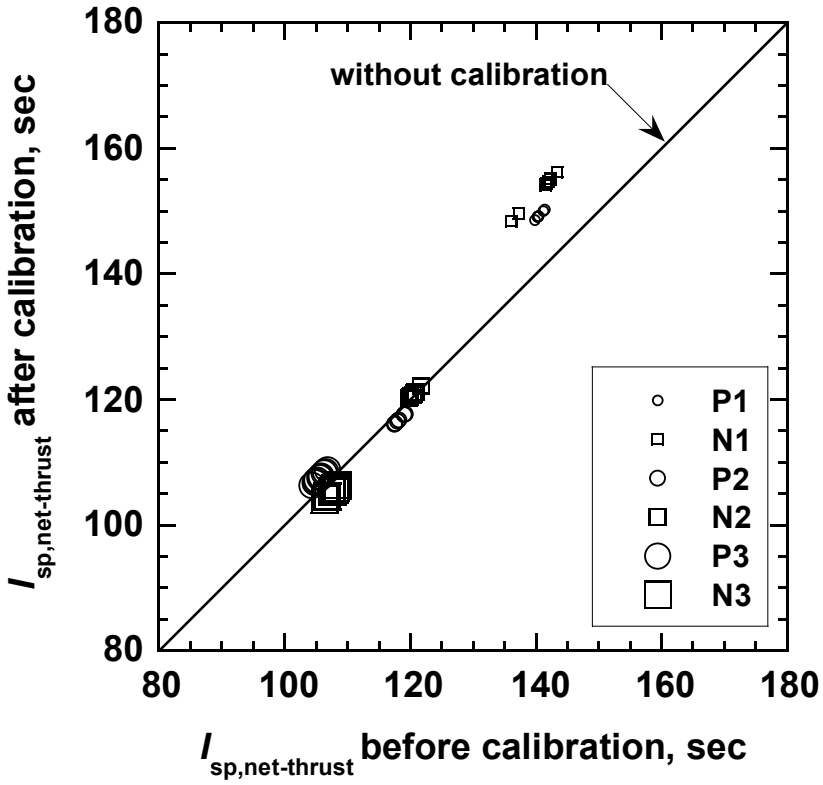

Fig. 7 Comparison of $I_{sp,net\text{-}thrust}$ between before and after calibration with the impactor

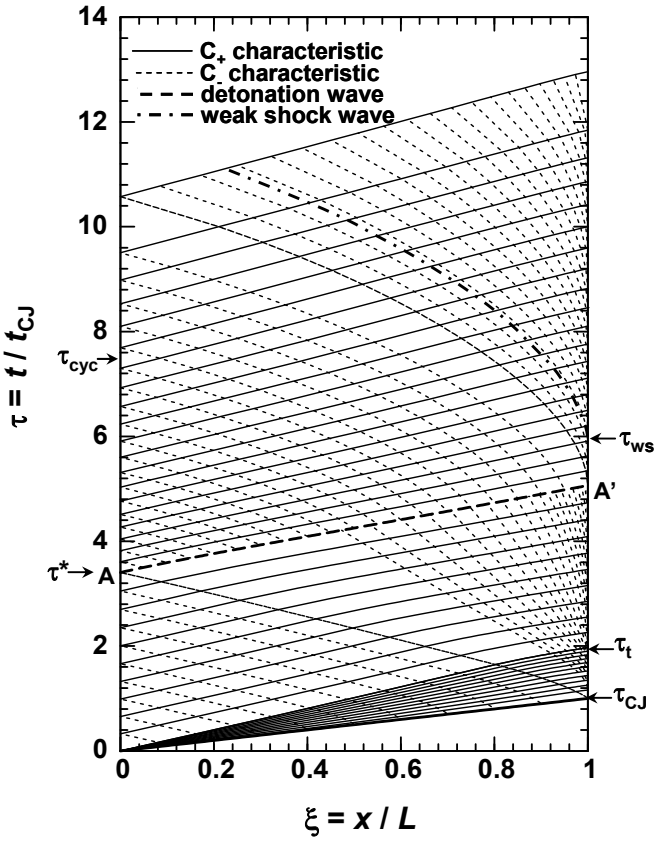

Fig. 8 Schematic ξ-τ diagram of characteristics.

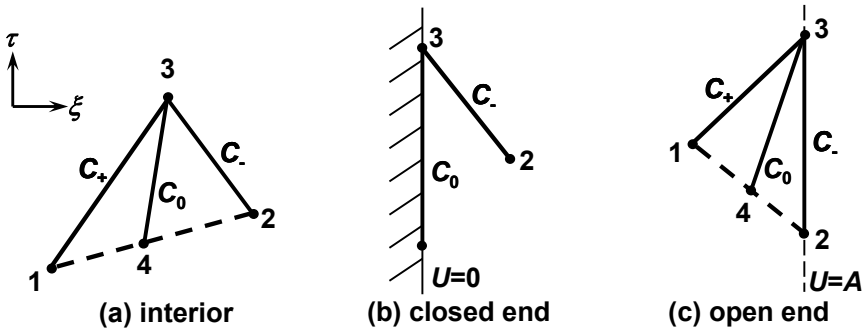

Fig. 9 Construction of the characteristics grid

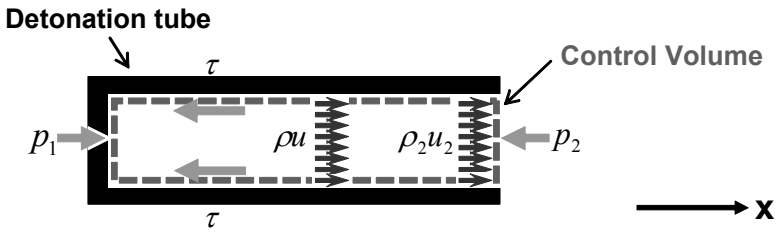

Fig. 10 Schematic diagram of control volume.

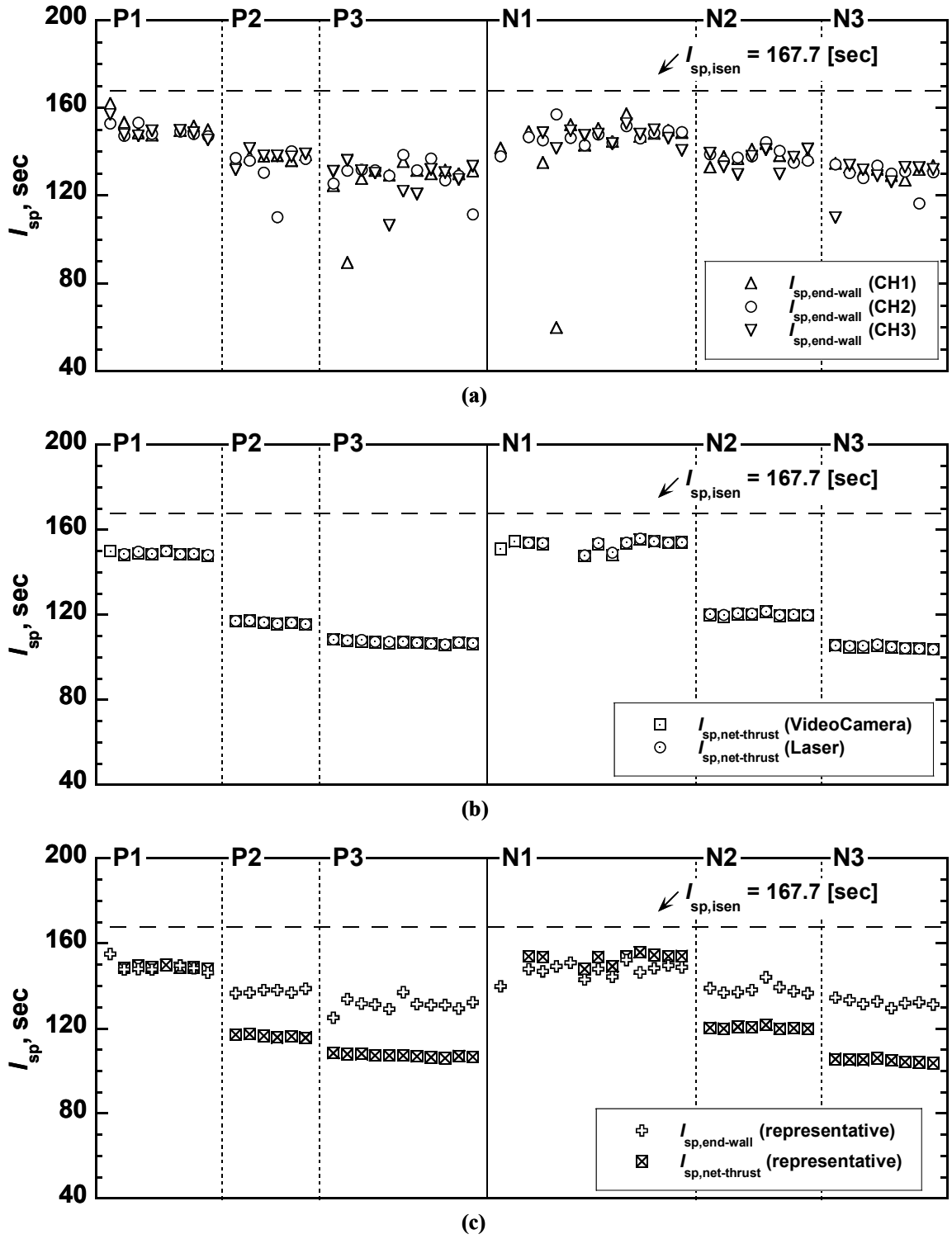

Fig. 11 Distribution of specific impulse for all shots carried out in the present study. Panel (a): pressure-based specific impulse. Panel (b): net specific impulse. Panel (c): representative specific impulse.

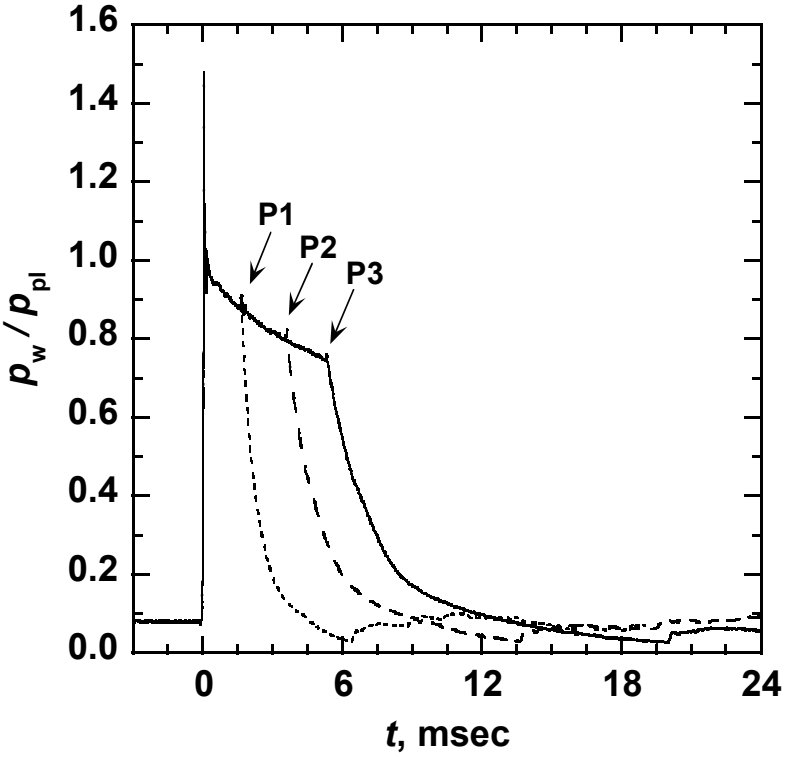

Fig. 12 Comparison between the pressure profiles obtained at the closed end of the polished tubes.

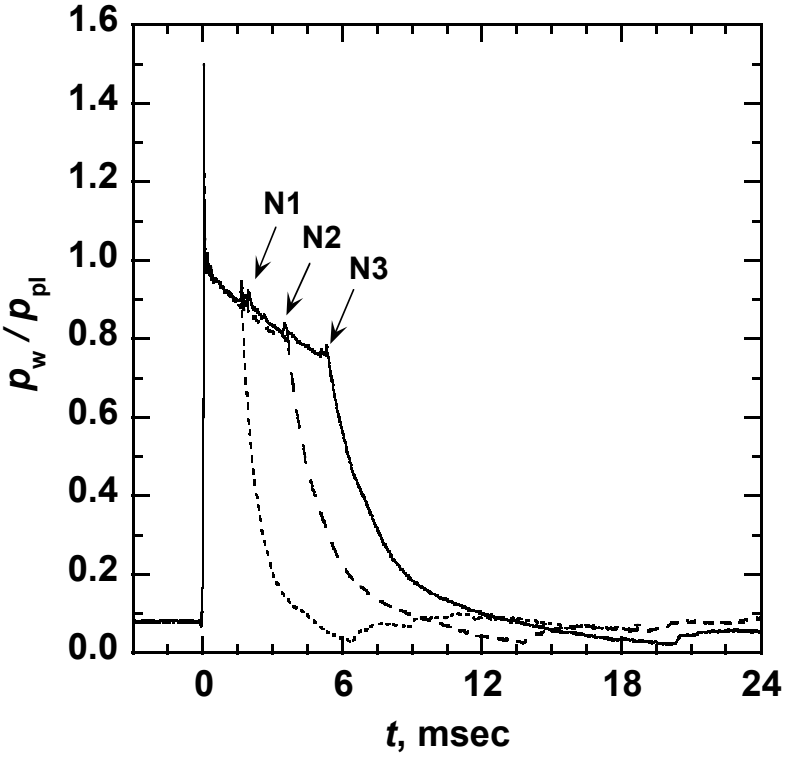

Fig. 13 Comparison between the pressure profiles obtained at the closed end of the normal tubes.

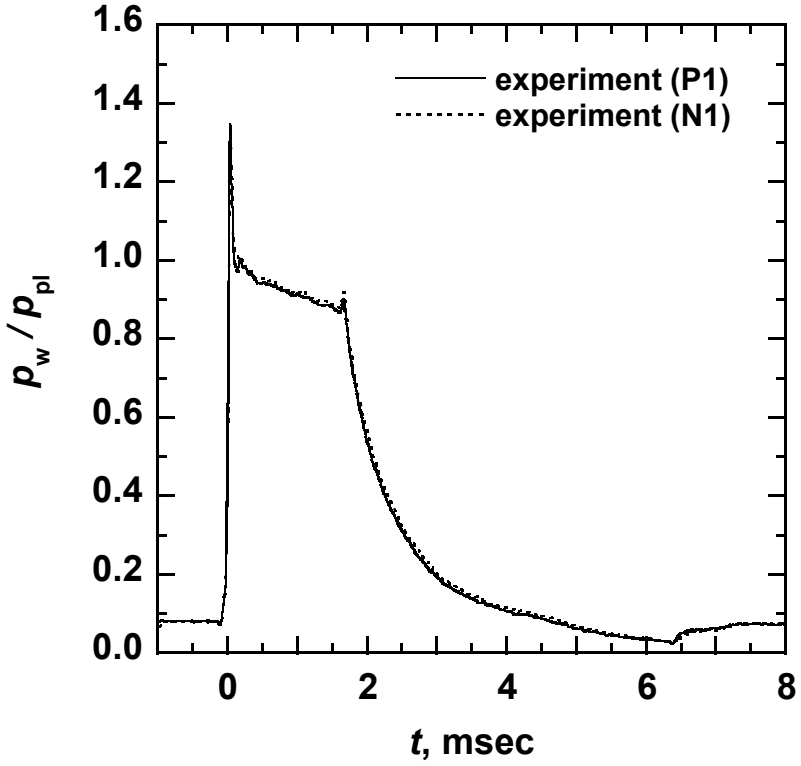

Fig. 14 Comparison between the pressure profiles obtained at the closed end of the tubes of L/D = 49.

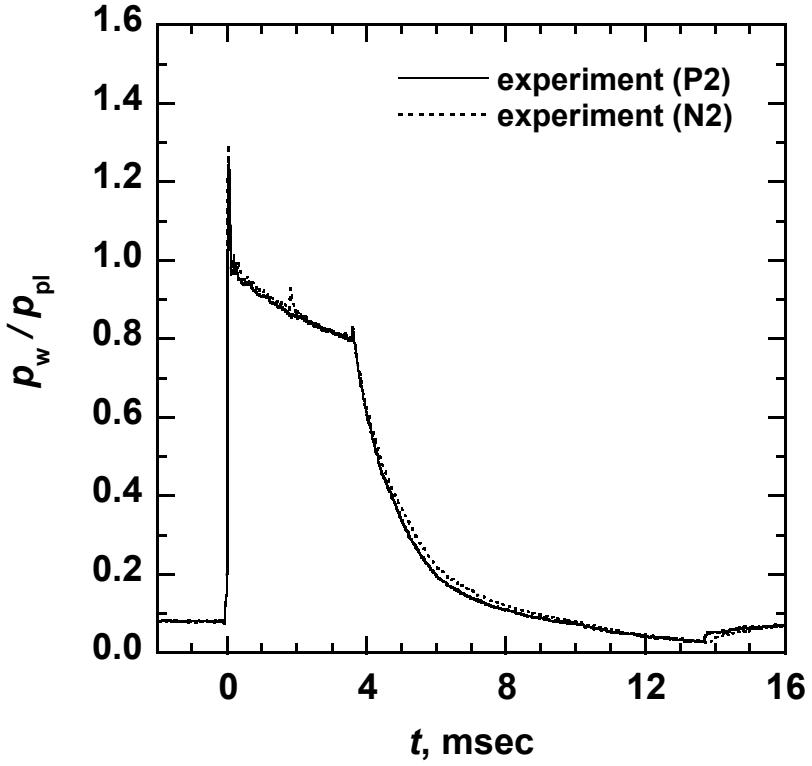

Fig. 15 Comparison between the pressure profiles obtained at the closed end of the tubes of L/D = 103.

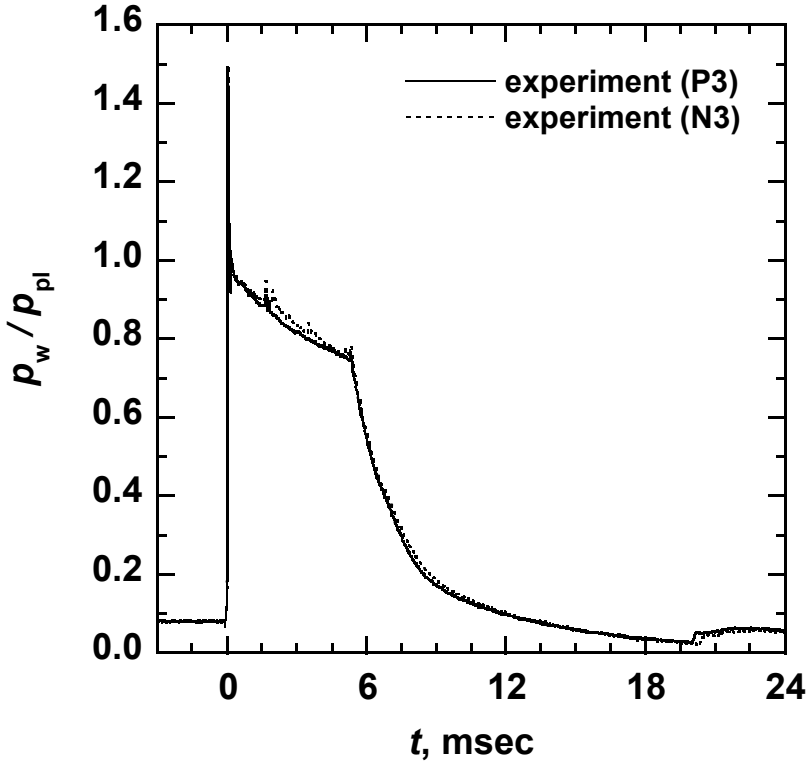

Fig. 16 Comparison between the pressure profiles obtained at the closed end of the tubes of L/D = 151.

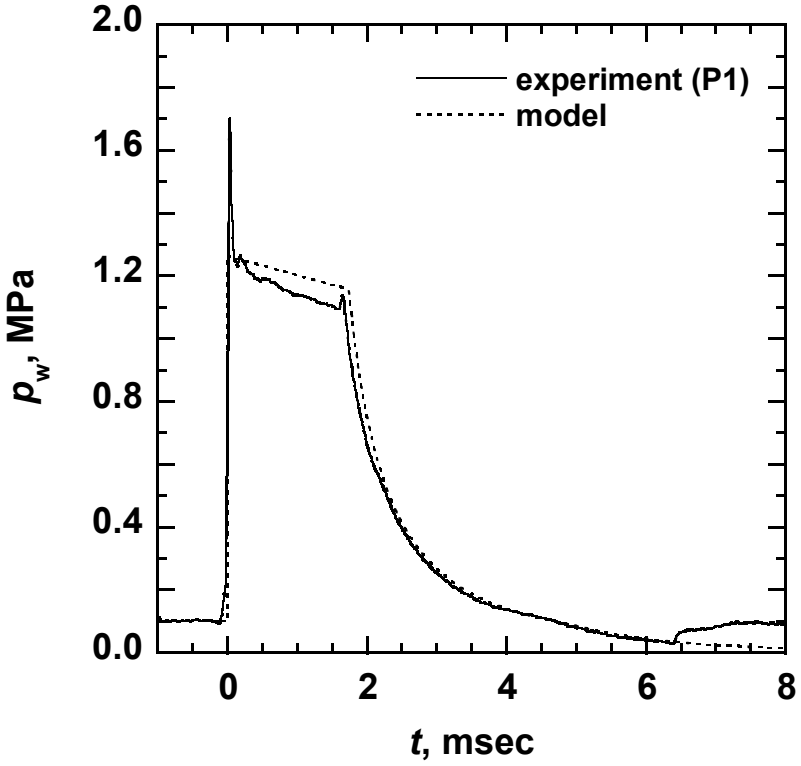

Fig. 17 Comparison between the experimental pressure profiles obtained at the closed end of tube P1 and the present model.

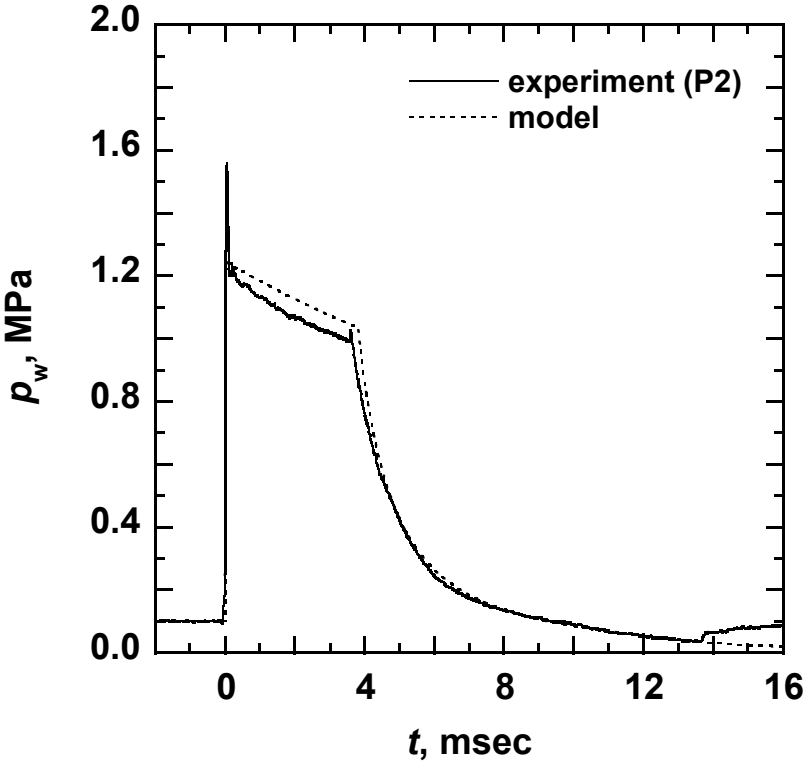

Fig. 18 Comparison between the experimental pressure profile obtained at the closed end of tube P2 and the present model.

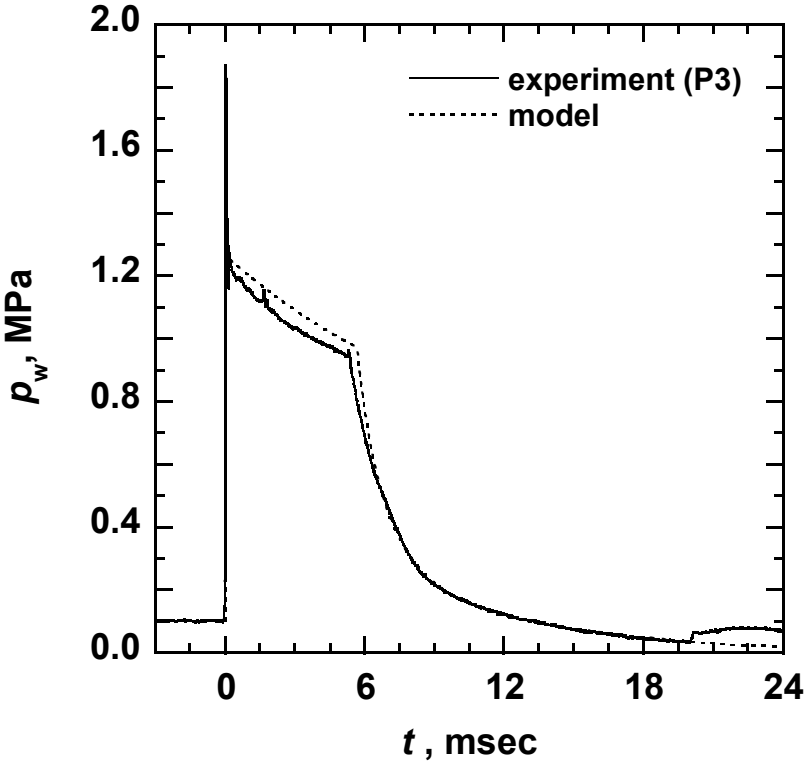

Fig. 19 Comparison between the experimental pressure profile obtained at the closed end of tube P3 and the present model.

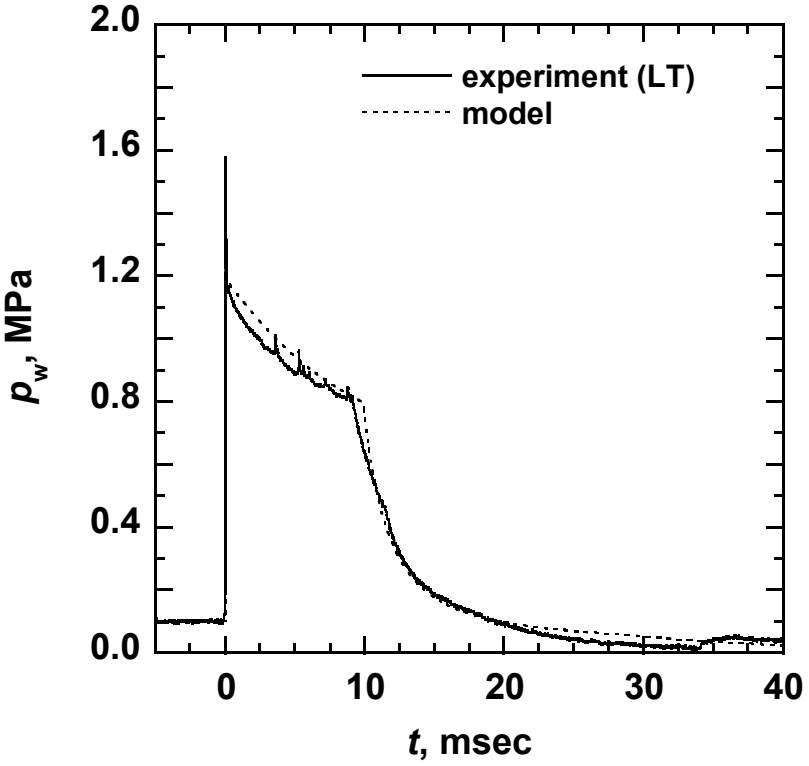

Fig. 20 Comparison between the experimental pressure profile obtained at the closed end of tube LT and the present model.

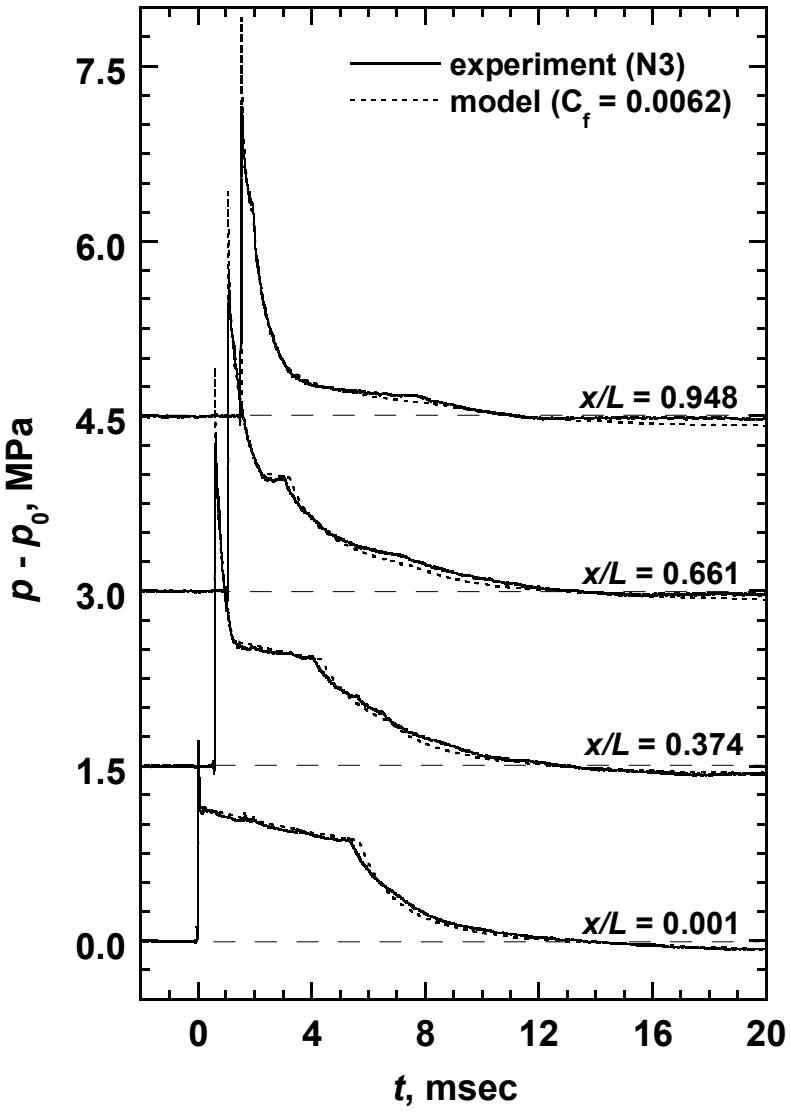

Fig. 21 **Comparison between the experimental pressure profiles measured at four different locations inside tube N3 and the present model; successive traces are shifted up by 1.5 MPa for clarity.**

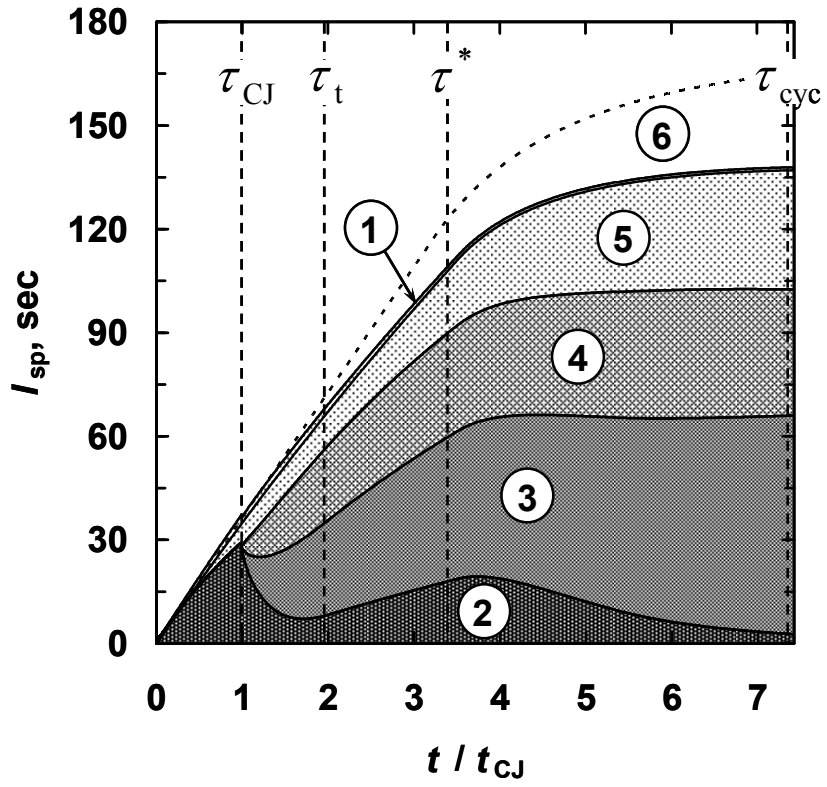

Fig. 22 Time histories of specific impulses in the case of P3.

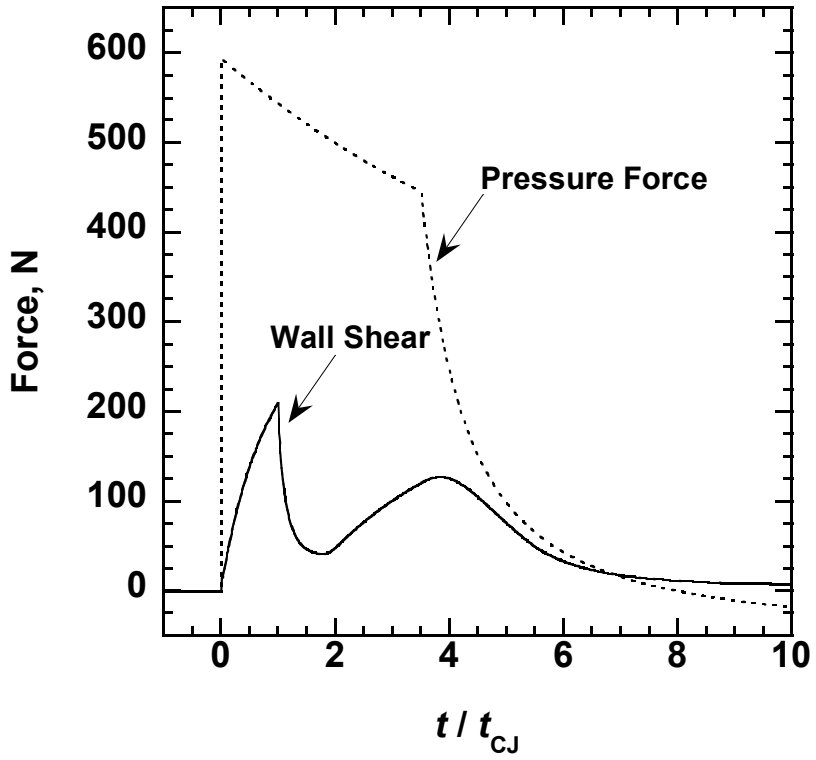

Fig. 23 Time histories of forces acting on the detonation tube in the case of P3.

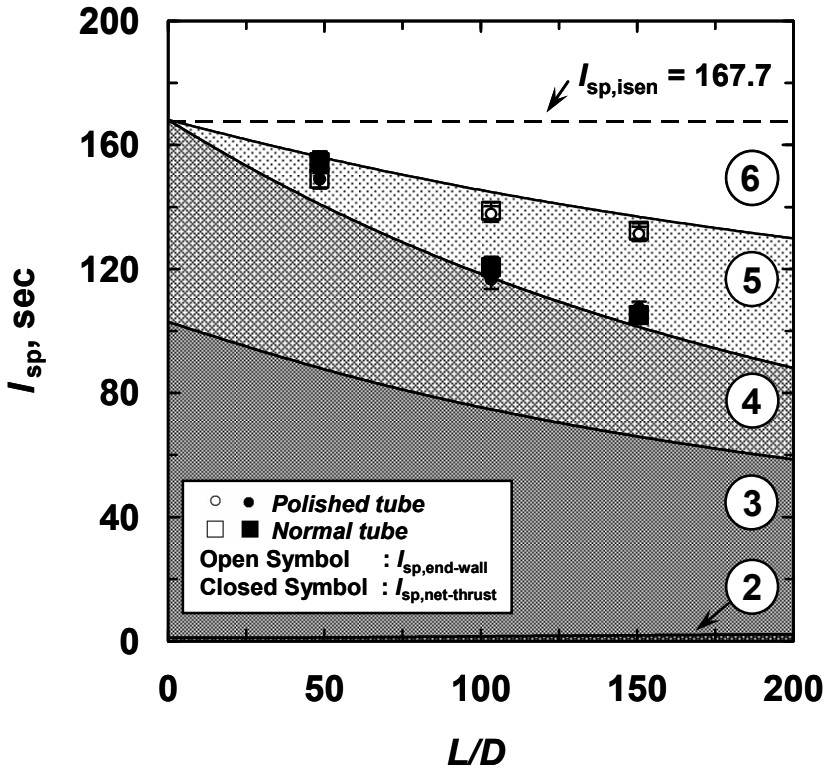

Fig. 24 Variation of specific impulse and its losses with *L*/*D* computed for C2H4+3O2 and comparison with experimental values